Modal Analysis of Receptivity Mechanisms for a Freestream Hot-Spot Perturbation on a Blunt Compression-Cone Boundary Layer

Michael Miselis*, Yuet Huang†, and Xiaolin Zhong‡
University of California, Los Angeles, California 90095

This work considers a theoretical approach to analyzing receptivity of a realistic geometry in hypersonic flow to a freestream entropy disturbance. Receptivity coefficients and phase angles are determined at a variety of locations by applying multimode decomposition to direct numerical simulation (DNS) data. The multimode decomposition scheme is implemented and rigorous verification performed against results from previous works. The method is then applied to the DNS results characterized by a freestream hotspot perturbation interacting with the bow-shock of Purdue's blunt compression cone in a Mach-6 freestream. The DNS data is decomposed into elements of the discrete and continuous spectra at various locations and frequencies, and the results compared to a prior, qualitative LST analysis. The previous analysis' conclusions are confirmed, showing that in the region downstream of the mode F / S synchronization location for the most unstable frequency, mode S is amplified and becomes the dominant mechanism of transition. The results upstream of this location are shown to be dominated by low frequency mode F perturbations. Receptivity coefficients are computed and examined for the branch I/II neutral frequencies at several locations. Brief continuous spectrum analysis is performed, showing agreement with previous work in the limited contribution from the entropy and vorticity spectra.

Nomenclature

$d()$	Perturbation of specified variable
e	Total energy per unit volume
f	Dimensional frequency, kHz
M_∞	Freestream Mach number
P	Pressure
Pr	Prandtl number
q_j	Heat flux due to thermal conduction
R^*	Gas constant
Re_∞/L	Freestream Reynolds number per unit length, 1/m
T	Temperature
T_r	Reference temperature
T_s	Sutherland's temperature
T_{wall}	Wall temperature
T_0	Total temperature
T_∞	Freestream temperature
u_1, u_2, u_3	Velocity components in the $\langle x_1, x_2, x_3 \rangle$ directions
U_∞	Freestream velocity
x^*	Position in streamwise direction, m

*Post-graduate Student, Mechanical and Aerospace Engineering Department
†Post-graduate Student, Mechanical and Aerospace Engineering Department
‡Professor, Mechanical and Aerospace Engineering Department, AIAA Associate Fellow.

α	Wavenumber in streamwise direction
β	Wavenumber in spanwise direction
γ	Specific heat ratio
μ	Viscosity
μ_r	Reference viscosity coefficient
ρ	Density
ρ_∞	Freestream density
τ_{ij}	Shear stress tensor
ξ	Natural coordinate along cone surface
η	Natural coordinate normal to the wall
ζ	Natural coordinate in azimuthal direction
ω	Circular frequency

I. Introduction

In designing hypersonic aerospace vehicles, the ability to predict the laminar-turbulent transition location on a body plays an extremely important role in aerodynamic heating analysis. Furthermore, when the vehicle is travelling in atmosphere at hypersonic speeds there exist weak disturbances in the freestream that can affect this transition location. The process whereby freestream disturbances induce laminar-turbulent transition can be divided into three stages: (i) boundary layer receptivity, (ii) linear eigenmode growth or transient growth, and (iii) nonlinear breakdown to turbulence.[1] Boundary layer receptivity is the process by which the freestream disturbances enter the boundary layer and generate instability waves - a preliminary stage by which laminar-turbulent transition occurs.[2,3]

Linear disturbance waves in a hypersonic boundary layer contain normal modes. The unstable modes were found by Mack, who indicated that the second mode is the dominant instability which leads to transition for flows with a Mach number higher than approximately four.[4,5] During hypersonic flight, the weak disturbances in the freestream are analogous to the linear disturbance waves; thus the second mode instability is particularly important to study. In addition, for a hypersonic flow, the bow-shock in front of a blunt nose creates entropy and vorticity layers, which are then swallowed by the boundary layer downstream.[3] The swallowing process of the entropy layer has a strong effect on boundary layer stability,[4] and the second mode instability can be affected by the entropy layer swallowing process.[4]

Kovasznay[6] stated that weak disturbances in compressible flow can be decomposed into acoustic, entropy and vorticity disturbances. McKenzie et al.[7] found that, regardless of the initial disturbance, acoustic, entropy and vorticity disturbances would always be generated behind the shock by the original disturbance's interaction with the shock. However, the mechanisms of the interaction of the various types of disturbances with the shock are individually different, leading to differences in the travelling angle and amplitude of the generated disturbances. In nature, the disturbances that exist in the freestream during atmospheric flight can consist of any of these three kinds. Consequently, detailed boundary layer receptivity studies for all three types of freestream disturbances and their interactions with a shock are necessary for complete understanding of the mechanism of hypersonic boundary layer receptivity over a blunt body. Freestream acoustic disturbance receptivity has been studied extensively,[8,9] and the use of laser equipment to generate a hotspot has been found to be a feasible way to impose non-acoustic freestream disturbances in a wind tunnel.[8,9] This provides sufficient justification for the use of a hotspot as the freestream disturbance in this paper.

The simulations in this paper have been coordinated with the experiments at Purdue University, and the schematic explanation of the laser-spot (hotspot) and cone scenario is demonstrated in Figure 1. The hotspot is generated at a location upstream of the cone on the centerline and convects with the hypersonic freestream toward the cone's nose. Eventually the spot interacts with and passes through the bow shock, traveling further downstream in the shock layer. The goal of this paper is to provide further analysis of the effects of a freestream hotspot perturbation on the growth of instability waves in the boundary layer behind the shock.

The compression cone, shown in Figure 2, is a cone with a circular base and circular-flared geometry along its body in the downstream direction. This geometry was expected to cause laminar-turbulent transition under quiet flow conditions due to the adverse pressure gradient that occurs along the flared portion of the

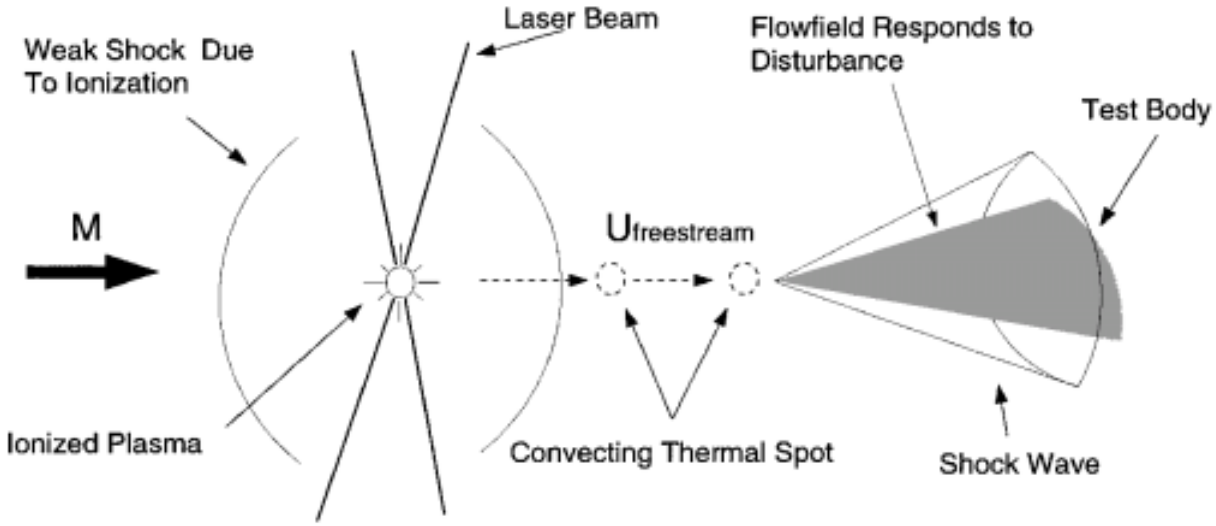

Figure 1: Schematic explanation of the laser-spot and cone scenario.[12]

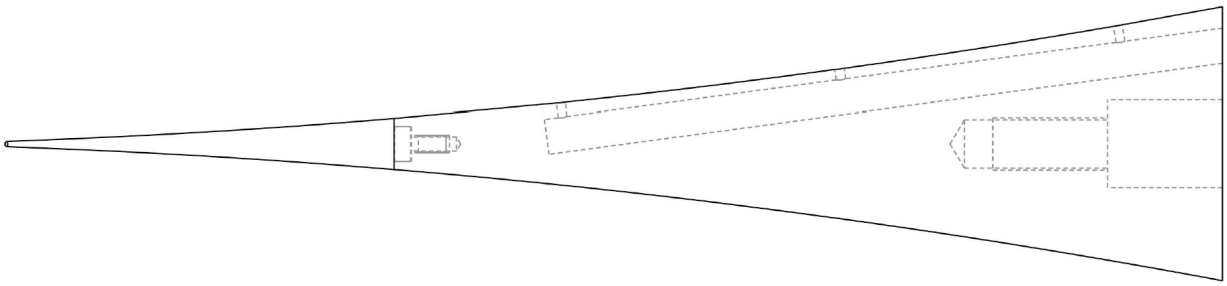

Figure 2: Schematic diagram of Purdue's Compression Cone.[10]

cone.[4,10] This adverse pressure gradient was verified in Huang & Zhong's mean flow DNS,[11] as shown in Figure 3. The aim of such geometry is to keep the boundary layer thickness constant in the downstream direction, such that a narrow range of unstable frequencies can be continuously amplified.[10]

The results of Huang & Zhong's 2010 hotspot DNS study[11] indicated that the freestream entropy perturbation would generate entropy and acoustic disturbances after passing through the bow shock. Furthermore, the acoustic disturbance behind the shock was seen to bounce back from the wall and interact with the bow shock again, generating further acoustic and entropy disturbances. Ma & Zhong[1] stated that when the acoustic waves generated from a freestream entropy perturbation and shock interaction reach the boundary layer, the perturbed boundary layer will reflect acoustic waves that then proceed to interact with the shock again, generating additional acoustic, entropy and vorticity disturbances. These additional disturbances, combined with the initial disturbances, propagate downstream and produce strong effects on receptivity. Ma & Zhong also performed a DNS study on a flat plate with freestream sinusoidal entropy waves at Mach 4.5. They found that the receptivity of the supersonic boundary layer to freestream entropy waves is essentially similar to the receptivity to freestream fast acoustic waves, wherein the fast acoustic waves generated behind the shock propagate downstream into the boundary layer to excite its instability modes. Ma & Zhong compared their simulation results with McKenzie et al.'s theoretical results, showing good agreement between the two.

In 2010, Huang & Zhong[11] completed the mean flow DNS using the shock-fitting method for a very blunt compression cone with a nose radius of $0.0127m$, as well as a sharper cone with nose radius of $0.001m$. In order to validate the resulting mean flow, a LST analysis was performed for the sharper cone mean flow, which showed an N-factor of 12.5, with the most amplified frequency $f = 278996\ Hz$. Both the LST

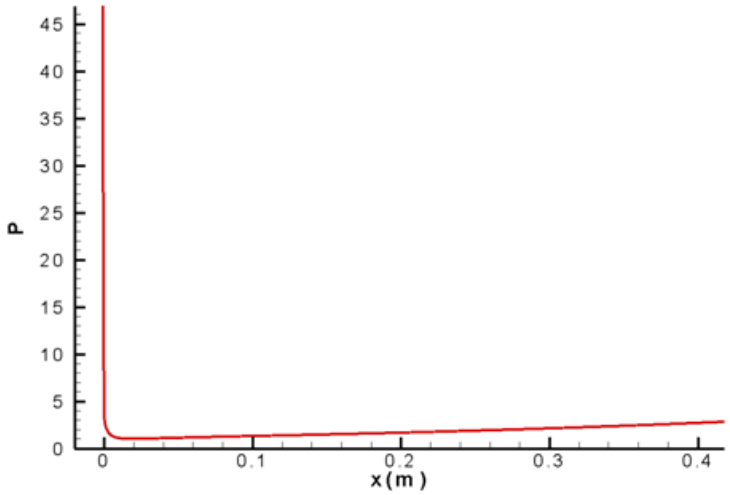

Figure 3: Pressure along the wall in case two.[11]

and shock-front position results agreed well with Purdue's shock-capturing DNS results. Huang & Zhong also developed a computer program for simulating the three dimensional hotspot perturbed flow behind a bow-shock. The program was further validated by computing the case for a freestream sinusoidal entropy wave, which obtained a qualitatively correct stagnation line perturbation distribution. Huang & Zhong also investigated the influence of the hotspot's size, computing two cases for freestream hotspots of very small radii.

In Huang & Zhong's 2011 analysis[13] of their hotspot DNS results, it was concluded that there was first mode growth at lower frequencies and second mode growth at higher frequencies, similar to the determination of their 2010 LST study.[11] This conclusion was reinforced by Huang & Zhong's 2014 analysis,[14] which determined that the second mode instability's growth was dominant in the region downstream of the most amplified frequency's mode F and mode S synchronization point. The second mode's amplification was identified to arise from the method of inter-modal exchange in the vicinity of this synchronization point. These analyses were facilitated by the comparison of LST and DNS results in regions dominated by the second mode instability.

In this paper, we intend to further investigate the receptivity of a boundary layer over a cone of realistic geometry to a realistic-sized freestream hotspot, corresponding to case A of Huang & Zhong's 2010 study.[11] Our goal is to apply an analysis to the data that is more rooted in the theoretical considerations of the problem, and to obtain the exact receptivity coefficients at any point of interest within the data set. This analysis is not possible through the application of LST alone to the DNS data, and we look to the method of multimode decomposition to enable this study.

Multimode decomposition for a compressible boundary layer was suggested through the 1983 work of Fedorov & Tumin[15] and further developed in rigor by Tumin in 2006[16] and 2007.[17] This method permits the filtering of individual modes from both the discrete (boundary layer) and continuous (freestream) spectra from a perturbation signal that comprises a sum of several such modes. This technique therefore enables the analysis of perturbation data even in regions where several modes of comparable amplitude coexist. This can be contrased with a pure LST analysis as was previously performed,[14] which relies largely on working backwards from LST mode shapes and parameters in order to compare these to DNS data. This LST analysis is therefore only feasible for regions where one mode is clearly asserted. In prior work, such as Tumin, Wang, & Zhong's 2007 analysis[18] and Denissen & White's 2009 study,[19] multimode decomposition was applied to similar DNS studies, with extensive verification performed to justify its utility.

In this work, we intend to implement the multimode decomposition scheme for a three-dimensional perturbation in a compressible, two-dimensional boundary layer as specified in Tumin's 2007 work.[17] To verify the implementation, extensive verification is to be performed against published results, previously

implemented methods, and the LST analysis specific to the DNS data to be analyzed.[14] With the method implemented and verified, we will then proceed to apply the technique to the DNS data for case A of Huang & Zhong's 2010 study. We intend to analyze the spatial evolution of the two boundary layer modes - mode F and mode S - and compare the results to the previous works' conclusions. Our final goal is the determination of the receptivity coefficients for the system at various locations, so that we may investigate their characterization of the system's receptivity to the freestream hotspot disturbance.

Although the method of multimode decomposition has seen limited application to DNS results, in many prior DNS analyses the determination of receptivity coefficients was not rigorous. This is especially true in cases where realistic geometries are examined, such as the blunt cone considered herein. With the ultimate goal being the characterization of flows for application in the development of hypersonic vehicles, it is thus an important step forward to apply the tools that have been developed to analysis of realistic cases. By implementing this tool in tandem with the DNS of receptivity for such systems, it is our hope that we may apply this to many such cases - and ultimately renew interest in a transition prediction tool that includes the effects of freestream amplitudes.

II. Direct Numerical Simulation

A. Governing Equations and Numerical Methods

The governing equations for DNS of hypersonic perfect-gas flow around a compression cone are given by the three-dimensional Navier-Stokes equations in conservative-law form and Cartesian coordinates:

$$\frac{\partial U}{\partial t} + \frac{\partial F_j}{\partial x_j} + \frac{\partial F_{vj}}{\partial x_j}, \quad j = 1, 2, 3 \tag{1}$$

The tensor notation, (x_1, x_2, x_3) represents the Cartesian coordinates, (x, y, z). The x axis points along the centerline of the cone from nose to rear, while the y axis points vertically upwards from the centerline of the cone, perpendicular to the x axis. The z axis is perpendicular to both x and y axes, pointing away from the centerline of the cone. Finally, the origin of the axes is at the center of the sphere that forms the cone's blunted nose. The vector U contains five conservative-law form dimensional flow variables:

$$U = \begin{bmatrix} \rho & \rho u_1 & \rho u_2 & \rho u_3 & e \end{bmatrix}$$

F_j and F_{vj} are the vectors of convective (inviscid) flux and viscous flux in j$^{\text{th}}$ spatial direction respectively:

$$\begin{aligned} F_j &= \begin{bmatrix} \rho u_j \\ \rho u_1 u_j + p\delta_{1j} \\ \rho u_2 u_j + p\delta_{2j} \\ \rho u_3 u_j + p\delta_{3j} \\ (e+p)u_j \end{bmatrix} \\ F_{vj} &= \begin{bmatrix} 0 \\ -\tau_{1j} \\ -\tau_{2j} \\ -\tau_{3j} \\ -\tau_{jk}u_k - q_j \end{bmatrix}, \quad k = 1, 2, 3 \end{aligned} \tag{2}$$

The equation of the state and the transport equations are:

$$\begin{aligned} p &= \rho R^* T \\ e &= \rho\left(c_v T + \frac{1}{2}u_k u_k\right) \\ \tau_{ij} &= \mu\left(\frac{\partial u_i}{\partial x_j} + \frac{\partial u_j}{\partial x_i}\right) - \lambda\frac{\partial u_k}{\partial x_k}\delta_{ij}, \quad \lambda = \frac{2}{3} \\ q_j &= -\kappa\frac{\partial T}{\partial x_j} \end{aligned} \tag{3}$$

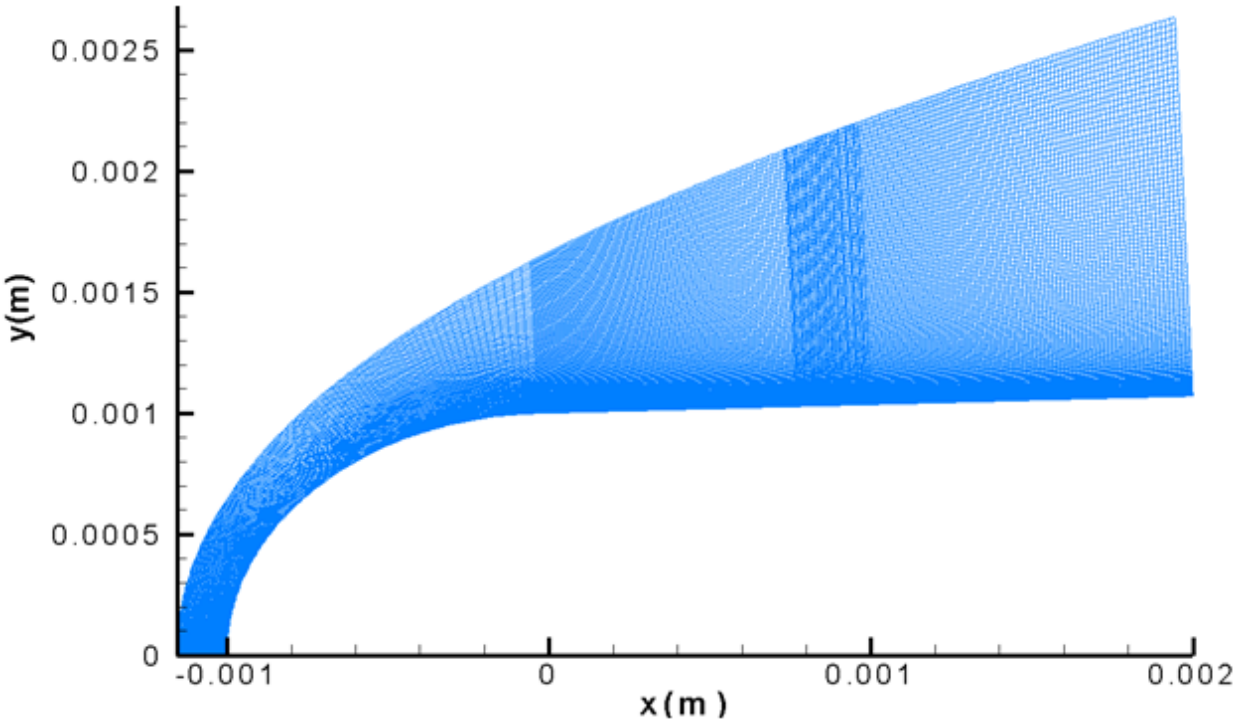

Figure 4: Partial view of grid configuration in zone 1, 2, and 3.

where R^* is the gas constant, and c_v is the specific heat, which is assumed to be constant with a given specific heat ratio γ. κ is the heat conductivity coefficient, which can be determined for a constant Prandtl number. The viscosity coefficient, μ, is approximated with Sutherland's law:

$$\mu = \mu_r \left(\frac{T}{T_0}\right)^{\frac{3}{2}} \left(\frac{T_r + T_s}{T + T_s}\right) \tag{4}$$

With this numerical implementation, the Cartesian Navier-Stokes equations are then transformed into body-fitted curvilinear computational domain coordinates (ξ, η, ζ) via a Jacobian matrix. The computational domain is bounded by the bow-shock and the wall of the cone - termed the 'shock-fitting' domain. The shock-fitting method can accurately resolve the position of the bow-shock, which is necessary for the high accuracy results required of receptivity and stability analyses. The shock-fitting grids move with time, and the motion is dependent on the shock position and shock velocity, with a partial view of the grid configuration shown in Figure 4. In each time-step, the shock's position and velocity are unknowns, and are determined by both freestream conditions and the solutions behind the shock. The spatial discretization of inviscid flux derivatives in the stream-wise (ξ) and wall-normal (η) directions are performed using a fifth-order finite-difference upwind scheme with local Lax-Friedrichs flux-splitting. A sixth-order central finite-difference scheme is used for viscous flux spatial derivatives. For spatial derivatives in the periodic azimuthal direction (ζ), Fourier collocation has been used, while Runge-Kutta is used for time-marching. The details of shock-fitting method, finite difference schemes and other numerical method implementations of the DNS are explained in Zhong's 1998 paper.[20]

B. Modeling Equations of Freestream Hotspot Perturbation

Physically, a hotspot is an entropy perturbation sphere surrounded by an acoustic perturbation (weak shock). The entropy core has Gaussian temperature and density distributions.[8,9] As in Huang & Zhong's 2010 paper,[11] the acoustic weak shock of a hotspot that is large compared to the cone's nose has very little influence. As such, the hotspot used in this consideration is modeled without the surrounding weak shock. As the initial position of the hotspot is 2cm upstream from the shock along the centerline in Dunn's paper,[21] the time scale required for the hotspot to diffuse and propagate in the freestream is very small relative to

the length scale of the initial distance between the center of hotspot and shock-front. Hence, it is reasonable to assume the hotspot profile remains unchanged when convecting with the freestream.

For the 3D hotspot model, the Gaussian perturbed freestream temperature is:

$$T = \Delta T_{max} exp\left(-\frac{R_c^2}{2\sigma^2}\right) + T_\infty \tag{5}$$

Thus, by the ideal gas law, the perturbed freestream density is:

$$\rho = \frac{p_\infty}{R\left(\Delta T_{max} exp\left(-\frac{R_c^2}{2\sigma^2}\right) + T_\infty\right)} \tag{6}$$

and the time derivative of the perturbed freestream density at the shock location is:

$$\frac{\partial \rho}{\partial \tau} = \left(\frac{p_\infty}{\sigma^2 R}\right)\frac{(T - T_\infty)}{T^2}\left[(X_c - U_\infty t)\left(\frac{\partial X_c}{\partial \tau} - U_\infty\right) + y_{shk}\frac{\partial y_{shk}}{\partial \tau} + z_{shk}\frac{\partial z_{shk}}{\partial \tau}\right] \tag{7}$$

where σ is the Gaussian shaping factor and τ is time in the computational domain. The initial difference in x-coordinate between the shock location and the center of the spot is:

$$X_c = |X_{spot} - x_{shk}| \tag{8}$$

where X_{spot} is the initial x-coordinate of the spot center, and x_{shk},y_{shk}, and z_{shk} are shock-front coordinates. Using the transport equation, the distance between the hotspot center and any point on the shock front at any time can be represented:

$$R_c = \sqrt{(X_c - U_\infty t)^2 + y_{shk}^2 + z_{shk}^2} \tag{9}$$

Where we note that the time in the computational domain is the same as time in physical domain.[20]

C. Boundary Layer Instability Spectral Analysis

The hotspot simulation is performed using the converged mean flow over the cone as a basis. The temporally varying boundary layer flow as the hotspot is passing through is recorded at a sufficiently well-resolved rate. The recorded boundary layer flow perturbations, however, are a combination of infinite frequency components. In this study, our main interest is in analyzing which frequencies excite instabilities in the boundary layer and how fast these instabilities grow spatially. Therefore, it is necessary to maintain a time-history of the boundary layer perturbations, which are then transformed to the frequency domain in order to study the behavior of the individual frequency components. This switch to the frequency domain is facilitated by Fourier transformation, which, for a flow variable $h(t)$ is defined as:[22]

$$H(f) = \int_{-\infty}^{\infty} h(t) e^{2\pi i f t} dt \tag{10}$$

where $h(t)$ is the variable's time function and $H(f)$ is its spectral value in frequency domain. Numerically, the continuous Fourier transform's spectral value can be approximated by:

$$H(f_n) \approx \Delta t \sum_{k=0}^{N-1} h_k e^{2\pi i k n/N} \tag{11}$$

where $H(f_n)$ is the spectral value at the n^{th} discretized frequency, N is the total number of Fourier collocation points used to discretize the time function $h(t)$, and h_k is the discretized time function. The spectral value, $H(f)$, has real and imaginary components in the frequency domain, while the magnitude of both is given by $|H(f)|$. In this paper, $h(t)$ is the time-history of the boundary layer perturbation, while $H(f)$ is the spectral value of the boundary layer perturbation in the frequency domain.

The transition to the frequency domain provides the discretized frequencies f_n and their associated values, $H(f_n)$, that determines the breadth our analysis. We define our remaining parameters relative to the frequency values determined above, with the discretized dimensionless frequency specified as:

$$F = \frac{2\pi\mu_\infty f}{\rho_\infty U_\infty^2} \tag{12}$$

The circular frequency is then defined based on this value:

$$\omega = Re \cdot F \tag{13}$$

where we specify the local Reynold's number, Re as:

$$Re = \frac{\rho_\infty U_\infty L^*}{\mu_\infty} \tag{14}$$

with reference length, L^*:

$$L^* = \sqrt{\frac{\mu_\infty \xi^*}{\rho_\infty U_\infty}} \tag{15}$$

D. Freestream Conditions and Compression Cone Geometries

The freestream conditions used in the numerical simulations in this paper are based on Purdue's Mach-6 Quiet Tunnel (BAM6QT):[10]

Table 1: Specified parameters for DNS and analysis

Parameter	Value
M_∞	6.0
T_0	433.0 K
T_r	288 K $(sea\ level)$
T_s	110.3 K $(sea\ level)$
T_{wall}	300.0 K
T_∞	52.8 K
Pr	0.72
R	287.04 $N \cdot m/kg \cdot K$ (air)
Re_∞/L	$1.026 \times 10^7 m^{-1}$
γ	1.4
ρ_∞	0.0403 kg/m^3
μ_r	1.7894×10^{-5} $kg/m \cdot s$ $(sea\ level)$
ϵ	0
β	0

The compression cone geometry is based on Schneider's design:[10]

$$\begin{aligned} &body - arc\ radius = 3.0m \\ &cone\ half - angle = 2.0^\circ \\ &cone\ length \approx 0.45m \\ &nose\ radius = 0.001m\ (Purdue's) \end{aligned}$$

The flow conditions and cone geometry are based on Purdue's experiment such that our simulation results can be compared with their experimental results. The nose radius is the same nose radius used in case 2 in Huang & Zhong's 2010 paper.[11]

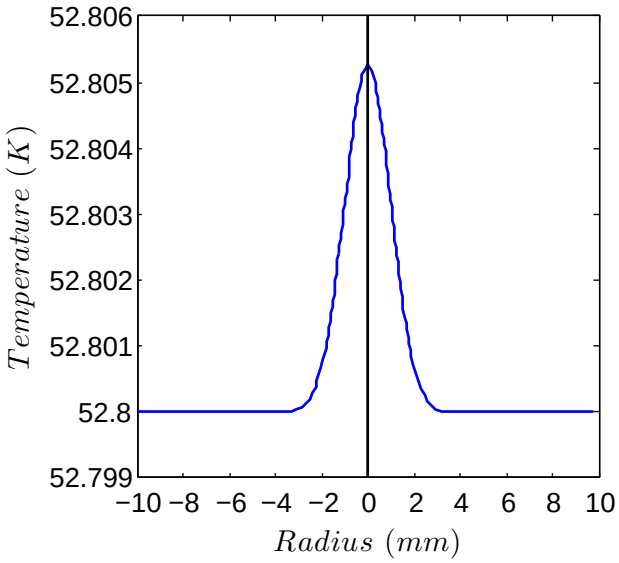

Figure 5: Gaussian distribution of perturbed temperature in the radial-direction.

E. Freestream Hotspot Parameters

The peak radius is controlled by the Gaussian factor, σ. In previous analysis,[11] three cases with different hotspot peak-region radii were analyzed. In this paper, the hotspot size is chosen to match the actual hotspot size in Purdue's experiments,[8,9] corresponding to case A from Huang & Zhong's 2010 study.[11]

$$\begin{aligned} &\sigma = 0.001 \;\; (largest\ radius: \;\; r = 0.003m) \\ &X_{spot} = -0.02m \end{aligned} \tag{16}$$

The hotspot perturbed flow simulated in this paper is based on the mean flow solution of case 2 in Huang & Zhong's 2010 work.[11] In order to keep the disturbance linear in the flow, the maximum temperature perturbation amplitude is chosen to be:

$$dT_{max} = T_\infty \times 10^{-4} = 0.00528 \ K \tag{17}$$

The profile of the hotspot's temperature distribution in the radial distribution is shown in Figure 5.

III. Theoretical Analysis

A. Problem Formulation

The theoretical analysis of the DNS results determined with the methods and conditions above is accomplished using the multimode decomposition technique for a three dimensional perturbation in a two dimensional boundary layer, as outlined by Tumin in 2007.[17]

The linearized Navier-Stokes equations for a two-dimensional, compressible boundary layer are rewritten in the non-conservative form:

$$\frac{\partial}{\partial y}\left(\mathbf{L}_0 + \frac{\partial \mathbf{A}^T}{\partial y}\right) + \mathbf{L}_1 \frac{\partial \mathbf{A}^T}{\partial y} = \mathbf{H}_1 \mathbf{A}^T + \mathbf{H}_2 \frac{\partial \mathbf{A}^T}{\partial x} + \mathbf{H}_3 \frac{\partial \mathbf{A}^T}{\partial z} \tag{18}$$

where $\mathbf{A}$ is specified as a row vector for consistency with the inner product definition below and has terms:

$$\mathbf{A}\,(x,y,z) = d\,[u, \partial u/\partial y, v, p, T, \partial T/\partial y, w, \partial w/\partial y, \partial u/\partial x, \partial v/\partial x, \partial T/\partial x, \partial w/\partial x, \partial u/\partial z, \partial v/\partial z, \partial T/\partial z, \partial w/\partial z]$$

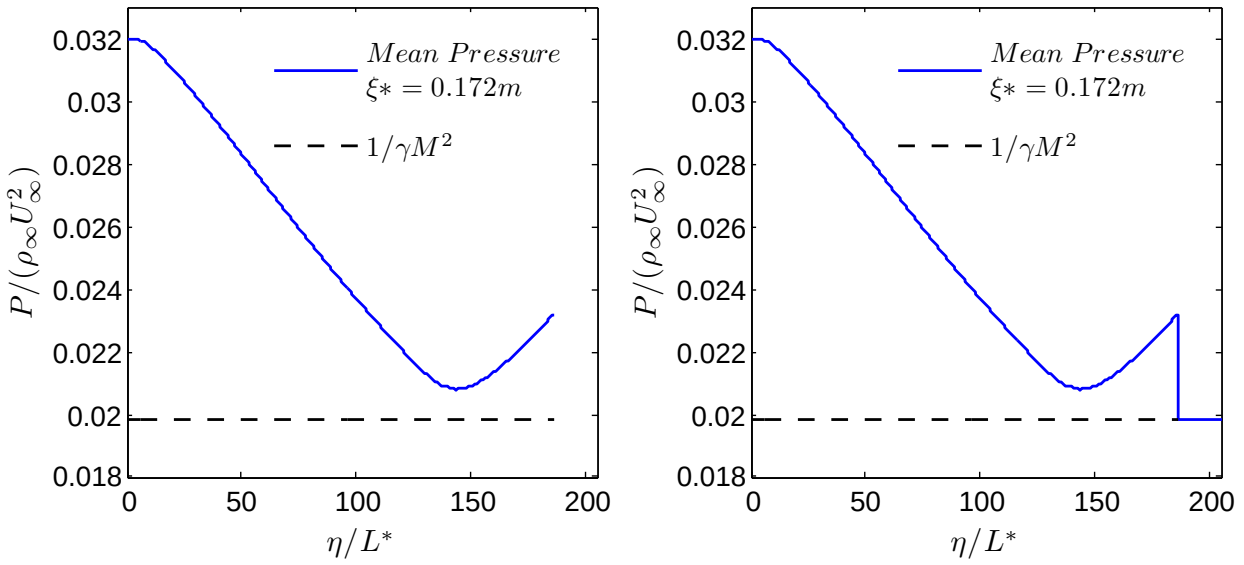

Figure 6: Meanflow pressure profile from DNS results (a) and with appended constant flow region outside of shock (b) at $\xi^* = 0.172m$.

where the d before the brackets indicates that the vector consists of perturbation values. $\mathbf{L}_0$, $\mathbf{L}_1$, $\mathbf{H}_1$, $\mathbf{H}_2$, and $\mathbf{H}_3$, are 16x16 matrices similar to those given in the reference work.[17] For the analysis of the DNS data over a compression cone, however, the typical assumption of constant meanflow pressure across the boundary layer was no longer applicable, with the discrepancy demonstrated by the meanflow pressure profile in Figure 6a. As such, the pressure terms and the relevant derivatives are reintroduced into the governing equations to account for the difference, and the appropriate adjustments made to the matrices $\mathbf{L}_0$, $\mathbf{L}_1$, $\mathbf{H}_1$, $\mathbf{H}_2$, and $\mathbf{H}_3$.

To the system of equations above, we apply a Fourier transform in z, and a Laplace transform in x, given by:

$$\mathbf{A}_{\alpha\beta} = \int_0^\infty e^{-px} \int_{-\infty}^\infty e^{-i\beta z} \mathbf{A}(x,y,z)\, dz\, dx \tag{19}$$

where $p = i\alpha$. The homogeneous component of the resulting system of equations takes the form:

$$\begin{gathered} \frac{\partial}{\partial y}\left(\mathbf{L}_0 \frac{\partial \mathbf{A}^T_{\alpha\beta}}{\partial y}\right) + \mathbf{L}_1 \frac{\partial \mathbf{A}^T_{\alpha\beta}}{\partial y} = \mathbf{H}_1 \mathbf{A}^T_{\alpha\beta} + i\alpha \mathbf{H}_2 \mathbf{A}^T_{\alpha\beta} + i\beta \mathbf{H}_3 \mathbf{A}^T_{\alpha\beta} \\ y = 0: \quad A_{\alpha\beta_j} = 0, \quad j = 1,3,5,7 \\ y \to \infty: \quad \left|A_{\alpha\beta_j}\right| < \infty, \quad j = 1,\ldots 16 \end{gathered} \tag{20}$$

For the system of equations above, the functional operator can be expressly defined:

$$\mathcal{L} = \frac{\partial}{\partial y}\left(\mathbf{L}_0 \frac{\partial}{\partial y}\right) + \mathbf{L}_1 \frac{\partial}{\partial y} - \mathbf{H}_1 - i\alpha \mathbf{H}_2 - i\beta \mathbf{H}_3 \tag{21}$$

In general, an adjoint operator, $\mathcal{L}^*$, is found from the definition:

$$\langle \mathcal{L}\boldsymbol{\mathcal{A}}, \boldsymbol{\mathcal{B}} \rangle = \langle \boldsymbol{\mathcal{A}}, \mathcal{L}^* \boldsymbol{\mathcal{B}} \rangle \tag{22}$$

The bracket notation above represents the Hermitian inner product on the range $[a,b]$,given as:

$$\langle \boldsymbol{\mathcal{A}}, \boldsymbol{\mathcal{B}} \rangle = \int_a^b \boldsymbol{\mathcal{A}}(y) \overline{\boldsymbol{\mathcal{B}}(y)}\, dy \tag{23}$$

where the overbar represents the complex conjugate of the term. The term $\boldsymbol{\mathcal{A}}(y)$ is specified as a row vector, while the term $\boldsymbol{\mathcal{B}}(y)$ is specified as a column vector. Thus, the term within the integral above is given as a dot product of two complex valued vectors. For convenience, we define our computational adjoint as the complex conjugate of the conventional adjoint:

$$\begin{aligned} \mathbf{A}_{\alpha\beta} &= \boldsymbol{\mathcal{A}}(y) \\ \mathbf{B}_{\alpha\beta} &= \overline{\boldsymbol{\mathcal{B}}(y)} \end{aligned} \tag{24}$$

Limiting our computational range to the region $[a, b] = [0, \infty)$, we substitute the above into the general definition of the adjoint and solve for $\mathcal{L}^*$:

$$\mathcal{L}^* = \frac{\partial}{\partial y}\left(\mathbf{L}_0^T \frac{\partial}{\partial y}\right) - \mathbf{L}_1^T \frac{\partial}{\partial y} - \mathbf{H}_1^T - i\alpha\mathbf{H}_2^T - i\beta\mathbf{H}_3^T \tag{25}$$

Thus, corresponding to the direct system of equations, there is an adjoint solution whose complex conjugate is determined by the set of equations:

$$\begin{gathered} \frac{\partial}{\partial y}\left(\mathbf{L}_0^T \frac{\partial \mathbf{B}_{\alpha\beta}}{\partial y}\right) - \mathbf{L}_1^T \frac{\partial \mathbf{B}_{\alpha\beta}}{\partial y} = \mathbf{H}_1^T \mathbf{B}_{\alpha\beta} + i\alpha\mathbf{H}_2^T \mathbf{B}_{\alpha\beta} + i\beta\mathbf{H}_3^T \mathbf{B}_{\alpha\beta} \\ y = 0: \quad B_{\alpha\beta_j} = 0, \quad j = 2, 4, 6, 8 \\ y \to \infty: \quad \left|B_{\alpha\beta_j}\right| < \infty, \quad j = 1, \ldots 16 \end{gathered} \tag{26}$$

The two systems of equations determined above can be rewritten as systems involving only the first eight elements of the vectors $\mathbf{A}_{\alpha\beta}$ and $\mathbf{B}_{\alpha\beta}$ respectively:

$$\begin{aligned} \frac{d\mathbf{z}_{\alpha\beta}^T}{dy} &= \mathbf{H}_0 \mathbf{z}_{\alpha\beta}^T \\ -\frac{d\mathbf{Y}_{\alpha\beta}}{dy} &= \mathbf{H}_0^T \mathbf{Y}_{\alpha\beta} \end{aligned} \tag{27}$$

where $\mathbf{H}_0$ is an 8x8 matrix, and $\mathbf{z}$ is the vector comprising the first 8 components of $\mathbf{A}_{\alpha\beta}$. As with the previously discussed matrices - $\mathbf{L}_0$, $\mathbf{L}_1$, $\mathbf{H}_1$, $\mathbf{H}_2$, and $\mathbf{H}_3$ - the terms in $\mathbf{H}_0$ are adjusted from the exact reference expressions by the inclusion of the pressure term and its derivatives. As $\mathbf{H}_0$ is the only matrix needed for the computational implementation carried out in this paper, the elements of $\mathbf{H}_0$ with meanflow pressure terms included are given in Appendix A.

The system of equations for $\mathbf{z}_{\alpha\beta}$ and $\mathbf{Y}_{\alpha\beta}$ above each have eight fundamental solutions, and the elements of the matrix $\mathbf{H}_0$ are constants in the freestream region where $d/dy \to 0$. Assuming fundamental solutions of the form $\mathbf{z}_{\alpha\beta}^{(j)} = \mathbf{z}_j^0 exp\left(\lambda_j y\right)$ permits the solution of the resulting eigenvalue problem for this region:

$$det\left(\mathbf{H}_0 - \lambda\mathbf{I}\right) = 0 \tag{28}$$

The eigenvalues and vectors in the freestream were re-derived for each j, and generally implemented as specified in the reference source.[17] The only exception was the self-referential element $z_{6j}^0 = \lambda_j z_{6j}^0$ which was determined as $z_{6j}^0 = \lambda_j z_{5j}^0$ instead. The fundamental solutions were also verified numerically, and, with the terms specified as such, the percent error for the systems of equations above was never observed in excess of approximately $10^{-6}\%$.

It is important to note that the DNS results determined using the methods prescribed in previous sections utilize a computational domain bounded by the bow-shock and the wall of the cone. As such, the results determined through DNS contain no true "freestream" region of constant meanflow. Consequently, in order to perform the integration, which must begin in a region of constant meanflow, an extra region with data equal to the far-field conditions of the problem is appended outside the bow shock that terminates the computational domain used in DNS. The shock is treated as infinitely thin, and the discontinuous transition from the DNS results to the far-field conditions is taken as consistent with the nature of the shock's effect on the flow field. The added region can be observed in Figure 6b, with the discontinuity present at $\eta/L^* \sim 180$.

Furthermore, in computing these freestream fundamental solutions for numerical integration, the exponential component of the solution is disregarded and only the vectors $\mathbf{z}_j^0$ considered. This is analogous to normalizing each fundamental solutions by the constant $exp(\lambda_j y_{fs})$, where y_{fs} is the point in the freestream

from which fundamental solution integration begins. Since the DNS freestream region is located outside of the shock, this ensures that the freestream values for the decaying fundamental solutions are computationally distinct from the null vector for the large values of y_{fs} required by the size of the DNS domain.

Continuing, the freestream fundamental solution vectors for the adjoint problem can be found using cofactors of the matrix of freestream fundamental solution vectors from the direct problem.[17,23] The typical formulae are given by:

$$C_{j,k} = (-1)^{j+k} \, det \left(\begin{bmatrix} m_{1,1} & \dots & m_{1,k-1} & m_{1,k+1} & \dots & m_{1,8} \\ \vdots & \ddots & \vdots & \vdots & \ddots & \vdots \\ m_{j-1,1} & \dots & m_{j-1,k-1} & m_{j-1,k+1} & \dots & m_{j-1,8} \\ m_{j+1,1} & \dots & m_{j+1,k-1} & m_{j+1,k+1} & \dots & m_{j+1,8} \\ \vdots & \ddots & \vdots & \vdots & \ddots & \vdots \\ m_{8,1} & \dots & m_{8,k-1} & m_{8,k+1} & \dots & m_{8,8} \end{bmatrix} \right) \tag{29}$$

$$adj\left(\mathbf{m}\right) = \mathbf{C}^T$$

where $\mathbf{C}$ is the cofactor matrix with elements $C_{j,k}$, and $\mathbf{m}$ is the matrix of freestream fundamental solution vectors for the direct problem. As described previously, each column of $\mathbf{m}$ is normalized by its respective exponential component:

$$\mathbf{m} = \left[\left(\mathbf{z}_1^0\right)^T, \left(\mathbf{z}_2^0\right)^T, \dots, \left(\mathbf{z}_8^0\right)^T \right] \tag{30}$$

With the freestream fundamental solution values known for both the direct and adjoint systems, it is then possible to begin numerical integration. To this effect, a classical Runge-Kutta (RK4) procedure was implemented according to the well-known method:[22]

$$\begin{aligned} k_1 &= hf\left(y_n, z_n\right) \\ k_2 &= hf\left(y_n + \frac{h}{2}, z_n + \frac{k_1}{2}\right) \\ k_3 &= hf\left(y_n + \frac{h}{2}, z_n + \frac{k_2}{2}\right) \\ k_4 &= hf\left(y_n + h, z_n + k_3\right) \\ z_{n+1} &= z_n + \frac{k_1}{6} + \frac{k_2}{3} + \frac{k_3}{3} + \frac{k_4}{6} + O\left(h^5\right) \end{aligned} \tag{31}$$

where, for the direct and adjoint cases respectively:

$$\begin{aligned} f\left(y_n, z_n\right) &= f\left(y_n, \mathbf{z}_{\alpha\beta_n}\right) = \mathbf{H}_0\left(y_n\right) \mathbf{z}_{\alpha\beta}^T\left(y_n\right) \\ f\left(y_n, z_n\right) &= f\left(y_n, \mathbf{Y}_{\alpha\beta_n}\right) = -\mathbf{H}_0^T\left(y_n\right) \mathbf{Y}_{\alpha\beta}\left(y_n\right) \end{aligned} \tag{32}$$

The integration is performed with a constant number of points in the wall-normal direction, with the step-size, h, dependent on the type of mode considered. For discrete modes, grid stretching was implemented to more accurately resolve the boundary layer region, while for continuous modes the step-size was constant to account for the oscillatory nature of solution in the freestream. The number of points used was $n_y = 3000$, determined by empirical observation of integration resolution. Accuracy is demonstrated by comparison of the solutions obtained to those from a doubled grid, as shown in Figures 7a and 7b.

The grid stretching used for the discrete modes is specified by mapping an evenly spaced computational domain, $0 \leq \eta \leq 1$, to the stretched domain $0 \leq y \leq y_{max}$:[24]

$$\begin{aligned} y &= \frac{a\eta}{b - \eta} \\ b &= 1 + \frac{a}{y_{max}} \\ a &= \frac{y_{max} y_i}{y_{max} - 2y_i} \end{aligned} \tag{33}$$

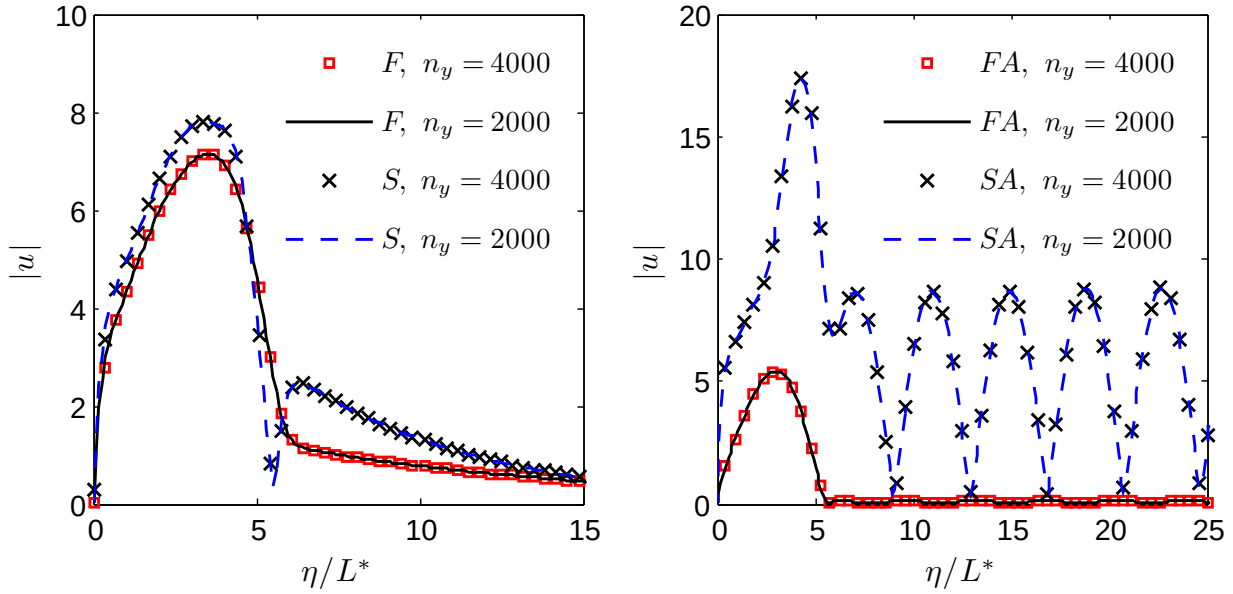

(a) (b)

Figure 7: Discrete mode F and mode S (a) and continuous fast acoustic and slow acoustic (b) results for $n_y = 2000$ vs. $n_y = 4000$. Flared cone conditions with $\xi^* = 0.398m$, $f = 139\ kHz$, and $k = 1$.

Where, for the grid stretching detailed above, half the grid points are placed between the wall and y_i, and y_i is specified as $y_i = 50$. Prior to integration of the freestream values, as well as after each integration step, the set of solution vectors for each problem was re-normalized to ensure orthogonality was maintained. For each location, the inverse of the transformations are then saved so that the results can be transformed back once integration is complete. The process is accomplished using QR factorization with a modified Gram-Schmidt orthonormalization technique.[25] The method can be described in brief as:

$$\mathbf{m} = \mathbf{QR} \tag{34}$$

where $\mathbf{m}$ is the matrix of fundamental solutions to be orthonormalized - either $\mathbf{z}^T_{\alpha\beta}(y_n)$ or $\mathbf{Y}_{\alpha\beta}(y_n)$, $\mathbf{Q}$ is the orthonormal system, and $\mathbf{R}$ is the transformation matrix, which records the transformations performed to orthonormalize the system. In detail, the matrices are computed as:

$$\begin{aligned} \mathbf{m} &= [a_1, \ldots, a_n, \ldots, a_k] \\ \mathbf{Q} &= [q_1, \ldots, q_n, \ldots, q_k] \end{aligned} \tag{35}$$

n=1	n=2	n=3	n=k
$u_1^{(0)} = a_1$	$u_2^{(0)} = a_2$	$u_3^{(0)} = a_3$	$u_k^{(0)} = a_k$
$q_1 = \frac{u_1^{(0)}}{\sqrt{\overline{u_1^{(0)}}^T u_1^{(0)}}}$	$u_2^{(1)} = u_2^{(0)} - \left[\overline{q_1}^T u_2^{(0)}\right] q_1$	$u_3^{(1)} = u_3^{(0)} - \left[\overline{q_1}^T u_3^{(0)}\right] q_1$	$u_k^{(1)} = u_k^{(0)} - \left[\overline{q_1}^T u_k^{(0)}\right] q_1$
	$q_2 = \frac{u_2^{(1)}}{\sqrt{\overline{u_2^{(1)}}^T u_2^{(1)}}}$	$u_3^{(2)} = u_3^{(1)} - \left[\overline{q_2}^T u_3^{(1)}\right] q_2$	$u_k^{(2)} = u_k^{(1)} - \left[\overline{q_2}^T u_k^{(1)}\right] q_2$

$$q_3 = \frac{u_3^{(2)}}{\sqrt{\overline{u_3^{(2)}}^T u_3^{(2)}}} \qquad \vdots$$

$$u_k^{(k-1)} = u_k^{(k-2)} - \left[\overline{q_{k-1}}^T u_k^{(k-2)}\right] q_{k-1}$$

$$q_k = \frac{u_k^{(k-1)}}{\sqrt{\overline{u_k^{(k-1)}}^T u_k^{(k-1)}}}$$

The method of orthonormalization described above is distinct from the classical Gram-Schmidt orthonormalization, with the difference engendered in the intermediate calculations for $u_k^{(k-1)}$. In the classical method, each vector is orthonormalized in one step as:

$$\begin{aligned} u_k &= a_k - \left[\overline{q_1}^T a_k\right] q_1 - \left[\overline{q_2}^T a_k\right] q_2 - \cdots - - \left[\overline{q_{k-1}}^T a_k\right] q_{k-1} \\ q_k &= \frac{u_k}{\sqrt{\overline{u_k}^T u_k}} \end{aligned} \tag{36}$$

While this method is much more condensed, the act of orthonormalizing the vector against $k-1$ dimensions at once can introduce rounding errors, with the result that the output vectors are not completely orthogonal. The modified method as described previously, however, orthogonalizes the vector against each dimension individually, with the result that each intermediate vector calculation $u_k^{(n)}$ is orthogonalized against the errors introduced during the calculations of $\left[u_k^{(1)}, \ldots, u_k^{(n-1)}\right]$.

As mentioned previously, the matrix $\mathbf{R}$ is also computed for each location, and is used to transform the solutions back to their previous state once numerical integration is complete. The matrix can be either determined numerically or specified analytically:

$$\mathbf{R} = \begin{bmatrix} \sqrt{\overline{u_1^{(0)}}^T u_1^{(0)}} & \overline{q_1}^T u_2^{(0)} & \overline{q_1}^T u_3^{(0)} & \cdots & \overline{q_1}^T u_k^{(0)} \\ 0 & \sqrt{\overline{u_2^{(1)}}^T u_2^{(1)}} & \overline{q_2}^T u_3^{(1)} & \cdots & \overline{q_2}^T u_k^{(1)} \\ 0 & 0 & \sqrt{\overline{u_3^{(2)}}^T u_3^{(2)}} & \cdots & \overline{q_3}^T u_k^{(2)} \\ \vdots & \vdots & \vdots & \ddots & \vdots \\ 0 & 0 & 0 & \cdots & \sqrt{\overline{u_k^{(k-1)}}^T u_k^{(k-1)}} \end{bmatrix} \tag{37}$$

Proceeding according to the method described above, the fundamental solutions can be computed numerically across the entirety of the boundary layer. The nature of these solutions, and how they are used, differs based on whether the mode being considered is an element of the discrete or continuous spectrum, with the case for each described in the following sections.

B. Discrete Modes

For discrete mode calculations, in keeping with the second boundary condition requirement for each system of equations above, the four fundamental solutions with exponentially growing values are not considered, and only those with decaying values are computed. By the principle of superposition, the solution to the system of equations for $\mathbf{z}_{\alpha\beta}$ and $\mathbf{Y}_{\alpha\beta}$ can be written as the sum of the decaying fundamental solutions for each system. We then have, according to the same fundamental solution indexing used in the reference:[17]

$$\begin{aligned} \mathbf{z}_{\alpha\beta} &= C_1 \mathbf{z}_{\alpha\beta}^{(1)} + C_3 \mathbf{z}_{\alpha\beta}^{(3)} + C_5 \mathbf{z}_{\alpha\beta}^{(5)} + C_7 \mathbf{z}_{\alpha\beta}^{(7)} \\ \mathbf{Y}_{\alpha\beta} &= C_2 \mathbf{Y}_{\alpha\beta}^{(2)} + C_4 \mathbf{z}_{\alpha\beta}^{(4)} + C_6 \mathbf{z}_{\alpha\beta}^{(6)} + C_8 \mathbf{z}_{\alpha\beta}^{(8)} \end{aligned} \tag{38}$$

The coefficients for $\mathbf{z}_{\alpha\beta}^{(k)}$ above are found by imposing the boundary conditions at the wall. To avoid a trivial solution, the boundary condition on temperature is omitted and instead the solution is normalized by the pressure at the wall. The wall temperature condition is instead imposed as a convergence criteria in the calculation of the spatial eigenvalue, α. As the same value of α is used for both the direct and adjoint solutions, the selection of the normalization variable for use in construction of the adjoint solution appears ambiguous, and is found to be arbitrary. In the results that follow, the wall value of the third element of the adjoint solution vector was selected as the normalization variable.

Though the coefficients are now determined at the wall, it remains to revert the orthonormalization performed during integration to obtain the fundamental solutions. This is accomplished by recognizing that, for a non-orthonormalized system, the constants used in the superposed solution will be identical to those determined at the wall throughout the entirety of the domain. Thus, in the vicinity of any point y_n where orthonormalization has been performed, we have:

$$\begin{aligned} f_n(y) &= \mathbf{Q}_n \mathbf{C}_n, \quad y_n - h \leq y \leq y_n \\ f_{n+1}(y) &= \mathbf{Q}_{n+1} \mathbf{C}_{n+1}, \quad y_n \leq y \leq y_n + h \end{aligned} \tag{39}$$

where $\mathbf{Q}_n$ is the matrix of orthonormalized solutions determined during numerical integration and $\mathbf{C}_n$ is the vector of coefficients for the fundamental solution superposition. Recognizing that at the point $y = y_n$, the solutions should be continuous:

$$\begin{aligned} \mathbf{Q}_n \mathbf{C}_n &= \mathbf{Q}_{n+1} \mathbf{C}_{n+1} \\ \mathbf{Q}_n &= \mathbf{m}_{n+1} \end{aligned} \tag{40}$$

Combining these two results and reducing yields:

$$\mathbf{C}_{n+1} = \mathbf{R}_{n+1} \mathbf{C}_n \tag{41}$$

As the coefficients are known at the wall, we can use this relation and the known transformation matrices $\mathbf{R}_n$ at each orthonormalization point to obtain coefficients across the domain. Combining the orthonormalized solutions at each point in proportion to the coefficients determined as above gives us the solutions corresponding to the system's discrete modes.

The solution for the full 16 element system $\mathbf{A}_{\alpha\beta}$ is found from that of the 8 element system $\mathbf{z}_{\alpha\beta}$ as:

$$\begin{aligned} \mathbf{A}_{\alpha\beta} = [&z_{\alpha\beta}(1), z_{\alpha\beta}(2), z_{\alpha\beta}(3), z_{\alpha\beta}(4), z_{\alpha\beta}(5), z_{\alpha\beta}(6), z_{\alpha\beta}(7), z_{\alpha\beta}(8), \\ &i\alpha z_{\alpha\beta}(1), i\alpha z_{\alpha\beta}(3), i\alpha z_{\alpha\beta}(5), i\alpha z_{\alpha\beta}(7), i\beta z_{\alpha\beta}(1), i\beta z_{\alpha\beta}(3), i\beta z_{\alpha\beta}(5), i\beta z_{\alpha\beta}(7)] \end{aligned} \tag{42}$$

while the full adjoint solution $\mathbf{B}_{\alpha\beta}$ is related to $\mathbf{Y}_{\alpha\beta}$ as specified in the reference.[17]

C. Continuous Modes

Continuous mode computations generally proceed in a manner analogous to the methods described above for discrete modes. The key difference relative to the discrete mode computation arises from the nature of the continuous spectrum as representing freestream modes that do not decay as $y \to \infty$. While the far-field boundary condition of the system requires that the solutions of Equation 20 and Equation 26 are bounded as $y \to \infty$, the condition imposed on discrete modes is more stringent - that is, that $\mathbf{z}_{\alpha\beta}^{(j)} \to 0$ and $\mathbf{Y}_{\alpha\beta}^{(j)} \to 0$ as $y \to \infty$. By expanding our consideration to fundamental solutions that are oscillatory at $y \to \infty$, the condition of boundedness is still satisfied, and a new class of solutions is available for consideration. By specifying α, it is possible to choose values such that $\lambda_{(2j-1,2j)}^2 = -k^2$ where $j = 1, 2, 3, 4$ and k is any real number with $Im(k) = 0$. This corresponds to enforcing that two fundamental solutions, $\mathbf{z}_{\alpha\beta}^{(2j-1,2j)}$ are proportional to $exp(\pm iky)$ and thus oscillatory as $y \to \infty$. The values of k can therefore be considered as wavenumbers for the oscillatory fundamental solutions in the wall-normal direction.

For the case where $\omega = 0$, there can be overlap of separate branches of the continuous spectrum, complicating the solutions in those regions. However, for the considerations of this paper, we are not concerned with stationary instabilities and thus disregard this case. The choice of j thus corresponds to the different branches of the continuous spectrum, while the selection of k corresponds to variations in α that describe the path of that continuous spectrum branch in the complex plane. The continuous spectrum branches are

characterized by their behavior in the freestream, with the acoustic branch related to pressure fluctuations, the vorticity branch corresponding to velocity perturbations, and the entropy branch corresponding to temperature and density perturbations . After specifying a particular branch for analysis through the choice of j, k is specified, with α determined from the definitions of the eigenvalues together with the equation $\lambda^2_{(2j-1,2j)} = -k^2$. Fundamental solution superposition then proceeds in a manner similar to the discrete modes, though with the inclusion of an additional solution:

$$\begin{aligned}\mathbf{z}_{\alpha\beta} &= C_1\mathbf{z}^{(1)}_{\alpha\beta} + C_3\mathbf{z}^{(3)}_{\alpha\beta} + C_5\mathbf{z}^{(5)}_{\alpha\beta} + C_7\mathbf{z}^{(7)}_{\alpha\beta} + C_{2j}\mathbf{z}^{(2j)}_{\alpha\beta} \\ \mathbf{Y}_{\alpha\beta} &= C_2\mathbf{Y}^{(2)}_{\alpha\beta} + C_4\mathbf{z}^{(4)}_{\alpha\beta} + C_6\mathbf{z}^{(6)}_{\alpha\beta} + C_8\mathbf{z}^{(8)}_{\alpha\beta} + C_{2j-1}\mathbf{z}^{(2j-1)}_{\alpha\beta}\end{aligned} \tag{43}$$

An exception to the equation above is required, however, due to the multiplicity of the eigenvalue pairs $\lambda_{1,2}$ and $\lambda_{7,8}$. When α is selected such that either of these pairs is oscillatory in the freestream, the other pair will similarly oscillate, and in these cases there are six bounded fundamental solutions but only five boundary conditions. The ambiguity here is resolved by analytical evaluation of the integrals along the branch cuts that comprise the continuous spectra in the complex plane. Analysis of these terms proceeds as in Tumin's 2006/2007 papers,[16,17] and the fundamental solutions for each of the two overlapped vorticity modes - A and B - are specified:

$$\begin{aligned}\mathbf{z}^{VA}_{\alpha\beta} &= C_1\mathbf{z}^{(1)}_{\alpha\beta} + C_2\mathbf{z}^{(2)}_{\alpha\beta} + C_3\mathbf{z}^{(3)}_{\alpha\beta} + C_5\mathbf{z}^{(5)}_{\alpha\beta} + C_8\mathbf{z}^{(8)}_{\alpha\beta} \\ \mathbf{Y}^{VA}_{\alpha\beta} &= C_1\mathbf{Y}^{(1)}_{\alpha\beta} + C_2\mathbf{z}^{(2)}_{\alpha\beta} + C_4\mathbf{z}^{(4)}_{\alpha\beta} + C_6\mathbf{z}^{(6)}_{\alpha\beta} + C_7\mathbf{z}^{(7)}_{\alpha\beta}\end{aligned} \tag{44}$$

$$\begin{aligned}\mathbf{z}^{VB}_{\alpha\beta} &= C_2\mathbf{z}^{(2)}_{\alpha\beta} + C_3\mathbf{z}^{(3)}_{\alpha\beta} + C_5\mathbf{z}^{(5)}_{\alpha\beta} + C_7\mathbf{z}^{(7)}_{\alpha\beta} + C_8\mathbf{z}^{(8)}_{\alpha\beta} \\ \mathbf{Y}^{VB}_{\alpha\beta} &= C_1\mathbf{Y}^{(1)}_{\alpha\beta} + C_4\mathbf{z}^{(4)}_{\alpha\beta} + C_6\mathbf{z}^{(6)}_{\alpha\beta} + C_7\mathbf{z}^{(7)}_{\alpha\beta} + C_8\mathbf{z}^{(8)}_{\alpha\beta}\end{aligned} \tag{45}$$

The determination of coefficients proceeds as before, however, an additional boundary condition is required due to the additional solution. Unlike the discrete modes, α is known prior to analysis, and thus the solutions are solved for directly with no need for iteration. The four wall boundary conditions can therefore be applied directly, along with an additional normalization condition. As above, unless otherwise stated we normalize each mode by the value of its pressure perturbation at the wall. The adjoint is determined similarly, where, as noted previously, we normalize by the wall value of element three of the adjoint solution vector.

With the coefficients at the wall thus determined, the corresponding coefficients of the orthonormalized system are determined at each orthonormalization point in the same manner as was done for the discrete modes, and the five fundamental solutions combined. Once completed, the systems are mapped to the full 16 element vectors $\mathbf{A}_{\alpha\beta}$ and $\mathbf{B}_{\alpha\beta}$. Our solutions thus computed, we are able to continue to the decomposition of the DNS signal into elements of these modes.

D. Biorthogonal Decomposition

It has been demonstrated in both the outlining source[17] as well as in Tumin and Fedorov's 1983 paper[15] that a solution to the linearized Navier-Stokes equation can be written as a summation of the solutions of both the normal and continuous spectra for that system:

$$\mathbf{A} = \sum_n C_n\mathbf{A}_{\alpha_n}(y)e^{i\alpha_n x} + \sum_j \int_0^\infty C_j\mathbf{A}_{\alpha_j}(y)e^{i\alpha_j(k)x}\,dk \tag{46}$$

where the first term represents summation over the discrete modes and the second term represents integration over the continuous modes. In the expression above, n represents the discrete modes which, for the purposes of this paper, are primarily limited to mode F and mode S, elsewhere referred to as the first and second Mack modes, while j represents the different types of continuous modes, i.e. vorticity, entropy, and acoustic. Together, the solutions $\mathbf{A}_{\alpha\beta}$ and $\mathbf{B}_{\alpha\beta}$ comprise the basis of the biorthogonal eigenfunction system.

We proceed to take the dot product of the system of equations for the direct problem $\mathbf{A}_{\alpha\beta}$, together with the adjoint solution, $\mathbf{B}_{\alpha'\beta}$, and integrate from $y = 0$ to $y = \infty$. Recognizing that α is not necessarily equal to α', we integrate by parts to find:

$$i\,(\alpha-\alpha')\int_0^\infty \left(\mathbf{H}_2\mathbf{A}^T_{\alpha\beta},\mathbf{B}_{\alpha'\beta}\right)\,dy=0 \tag{47}$$

This orthogonality relation can then be rewritten in the more explicit form:

$$\langle\mathbf{H}_2\mathbf{A}^T_{\alpha\beta},\mathbf{B}_{\alpha'\beta}\rangle=\int_0^\infty\left(\left(\mathbf{H}_2\mathbf{A}^T_{\alpha\beta}\right)^T,\mathbf{B}_{\alpha'\beta}\right)\,dy=\Gamma\Delta_{\alpha\alpha'} \tag{48}$$

The bracketed terms indicate the inner product, while the term $\Delta_{\alpha\alpha'}$ is either a Kronecker delta if α or α' are eigenvalues of the discrete spectrum, or a Dirac delta if both α and α' are eigenvalues of the continuous spectrum. The term Γ depends on the normalization of $\mathbf{A}_{\alpha\beta}$ and $\mathbf{B}_{\alpha'\beta}$, where in our case $\mathbf{A}_{\alpha\beta}$ is normalized by the pressure values at the wall and $\mathbf{B}_{\alpha'\beta}$ is normalized by the third element of the adjoint solution vector, as specified above. In the analysis performed below, the term Γ was determined by letting $\alpha=\alpha'$ and calculating the inner product numerically according to the equation above.

With the help of this orthogonality relation, and by substituting in the definition of $\mathbf{A}$ given by Equation 46, we can calculate the values of the coefficients, C, as:

$$C=\frac{\langle\mathbf{H}_2\mathbf{A},\mathbf{B}_{\alpha\beta}\rangle}{\Gamma}e^{-i\alpha x} \tag{49}$$

In particular, as we are interested in calculating the coefficients of modes contained within the DNS data, we have:[18]

$$C_{DNS}=\frac{\langle\mathbf{H}_2\mathbf{A}_{DNS},\mathbf{B}_{\alpha\beta}\rangle}{\Gamma}e^{-i\alpha x_{DNS}} \tag{50}$$

In this case, where we have the exact DNS data available across the entirety of the domain, we concern ourselves primarily with the local amplitude rather than spatial evolution and so set $x_{DNS}=0$ to recover the values. Although the method described above and implemented in the following analysis is appropriate for a three dimensional perturbation, the DNS results analyzed are characterized by a two-dimensional perturbation, and the spanwise wavenumber, β, is specified as zero accordingly.

IV. Theoretical Boundary Layer Receptivity Verification

The theoretical analysis of the DNS data obtained was performed using the multimode decomposition scheme outlined in Section III above. Prior to performing this analysis, however, extensive verification was attempted using the figures and data available from relevant sources.[14,16,17]

The first phase of verification was ensuring that the eigenfunctions of both the continuous and discrete spectra were computed accurately. These eigenfunctions are necessary for determining the mode amplitude coefficients, as they comprise the $\mathbf{A}_{\alpha\beta}$ terms that are used in equations above. Furthermore, accurate determination of the spatial eigenvalue α, is necessary for the computation of both the discrete and continuous eigenfunctions. Thus, a comparison of these eigenfunctions to those from previous work ensures the accurate determination of both the eigenvalues and eigenfunctions of these modes.

Unlike the analysis of the DNS data, for these verification cases the meanflow pressure was assumed constant and equal to $1/\gamma M^2$ while the pressure derivatives were set to zero, consistent with the boundary layer assumption and the non-dimensionalization used.[24] Thus, these computations also served to verify that the derived system of equations correctly reduces when assigned a constant pressure meanflow profile.

Being arguably the simplest of the two mode types both in concept and implementation, the discrete spectrum was selected as our first means of verification. Through prior work, a second order finite difference (2FD) scheme had been implemented for the determination of global eigenvalue spectra, along with a fourth order compact difference (4CD) scheme for local eigenvalue searches. These two routines were implemented in accordance with the framework laid out in Malik's 1990 paper,[24] and were tested against the results from Balakumar and Malik's 1992 paper,[26] with the results presented in Table 3 and Table 4. Once verified, these routines were used as the baseline for comparing our implementation of the fundamental solution superposition method for discrete modes. The comparison between eigenfunction results for both schema is illustrated in Figure 8. Having verified the global second-order finite difference method and fourth order compact difference scheme, these were later used in the DNS analysis to obtain initial guesses for the discrete

Table 3: Flat plate, $M = 4.5,\ T_0 = 311\ K,\ Pr = 0.72,\ Re = 1000,\ \omega = 0.2,\ \beta = 0$

Balakumar, Malik	2FD	4CD	Fund. Soln. Superposition
$0.220 - i3.091 \times 10^{-3}$	$0.220 - i3.486 \times 10^{-3}$	$0.220 - i3.091 \times 10^{-3}$	$0.220 - i3.091 \times 10^{-3}$
$0.221 - i1.569 \times 10^{-2}$	$0.221 - i1.484 \times 10^{-2}$	$0.221 - i1.569 \times 10^{-2}$	$0.221 - i1.570 \times 10^{-2}$
$-0.565 - i5.559 \times 10^{-2}$	$-0.561 - i6.767 \times 10^{-2}$	$-0.565 - i5.560 \times 10^{-2}$	$-0.565 - i5.560 \times 10^{-2}$
$0.560 - i5.659 \times 10^{-1}$	$0.610 - i5.824 \times 10^{-1}$	$0.560 - i5.636 \times 10^{-1}$	$0.561 - i5.660 \times 10^{-1}$

Table 4: Flat plate, $M = 4.5,\ T_0 = 311\ K,\ Pr = 0.72,\ Re = 1000,\ \omega = 0.2,\ \beta = 0.12$

Balakumar, Malik	2FD	4CD	Fund. Soln. Superposition
$0.2181 + i2.969 \times 10^{-4}$	$0.2179 + i9.464 \times 10^{-5}$	$0.2181 + i2.971 \times 10^{-4}$	$0.2181 + i2.973 \times 10^{-4}$
$0.2124 + i1.288 \times 10^{-2}$	$0.2129 + i1.194 \times 10^{-2}$	$0.2124 + i1.288 \times 10^{-2}$	$0.2124 + i1.288 \times 10^{-2}$
$-0.5498 + i5.684 \times 10^{-2}$	$-0.5457 + i6.850 \times 10^{-2}$	$-0.5499 + i5.685 \times 10^{-2}$	$-0.5499 + i5.685 \times 10^{-2}$

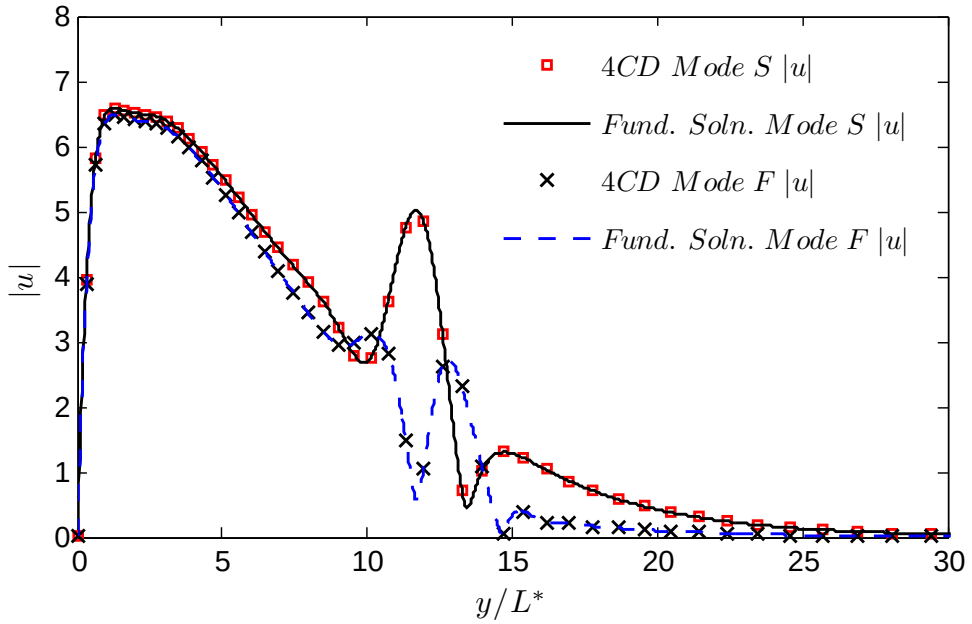

Figure 8: Comparison of eigenfunctions from fourth-order compact difference scheme and fundamental solution superposition. Flat plate, $M = 4.5,\ T_0 = 311\ K,\ Pr = 0.72,\ Re = 1000,\ \omega = 0.2,\ \beta = 0.12$.

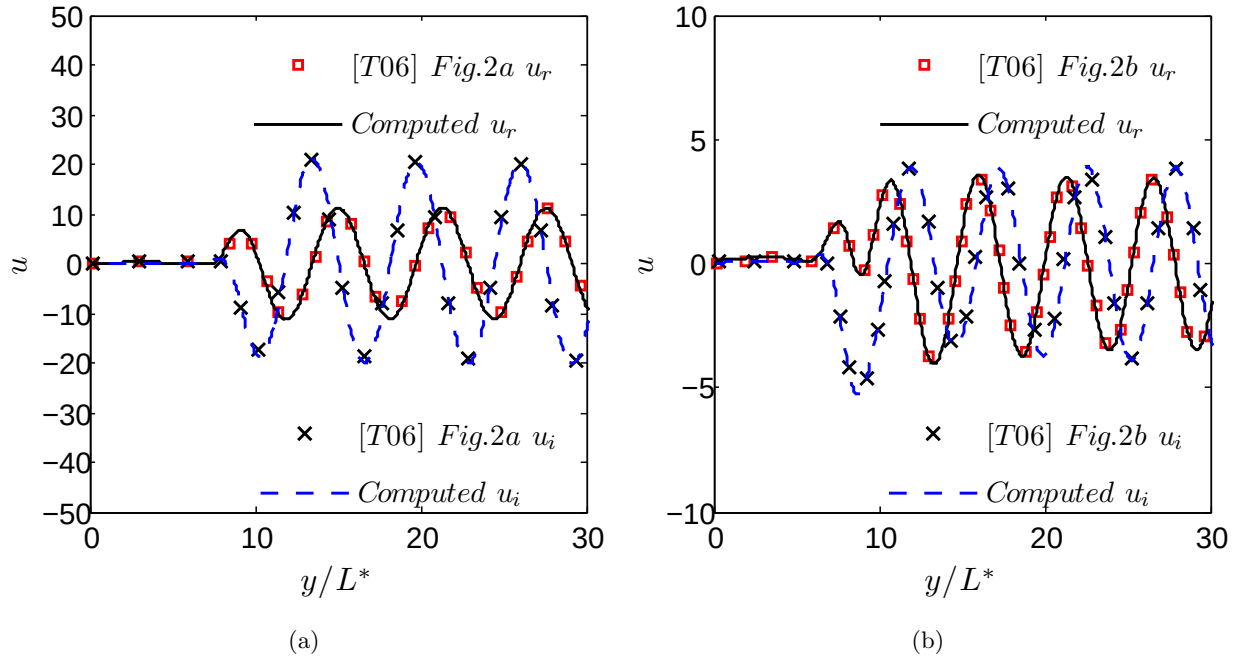

Figure 9: Comparisons of continuous vorticity mode A (a) and continuous entropy mode (b) from Fig. 2 of reference T06[16] to computed values, $M = 5.95,\ T_w/T_{ad} = 0.1,\ F = 10^{-4},\ Re = 1500,\ \beta = 0.16,\ k = 1.$

mode eigenvalues. The values obtained with these techniques were then refined with the fundamental solution integration method.

The results for our implementation of the fundamental solution superposition technique were also tested against those presented in Tumin's 2006 work.[16] As in the source, the eigenfunctions are normalized by the derivative of streamwise velocity at the wall, rather than the pressure at the wall as is the general case throughout this paper. The results are presented in Figures 9-15 with both continuous and discrete modes represented. For the continuous modes, the value of the parameter k is set to 1 in each case. In most of these cases, the stagnation temperature was not specified in the source. By matching eigenfunction profiles it was found that $T_0 = 640\ K$ was the best estimate, and this is the specification used unless otherwise noted. Figures 9-13 show comparisons to plots given in Tumin's 2006 paper,[16] abbreviated as [$T06$], with the source figure cited in the legend.

In the majority of these comparisons the agreement is near exact, with some error attributable to the hand digitization of the verified plots. One exception is Figure 11b, where the source indicates a coefficient $C_V = 2$ for the continuous vorticity mode. It was found, however, that the calculated values compare much more closely when a coefficient of $C_V = 1$ is used. The computed values shown in the plot thus include the case where $C_V = 1$, and it is presumed that the coefficient claimed in the source is erroneous. This assumption is bolstered by the comparisons shown in Figures 9a and 12b, which both include continuous vorticity modes of weight $C_V = 1$ and $C_V = 0.1$ respectively. These figures rely on similar calculations - the only difference being the flow conditions - and show excellent comparison to the source plots. A similar issue is also noted in Figures 13a and 13b, where the source claims a mode sum with the weights $C_S = 1$, $C_F = -1$, and $C_{continuous} = 2$ for each, with the continuous spectrum mode being fast acoustic for Figure 13a and slow acoustic for Figure 13b. Better accuracy was noted, however, when the coefficients of the two discrete modes are switched, with $C_S = -1$ and $C_F = 1$ for both cases. The two modes were identified as indicated in the global eigenvalue spectrum shown in Figure 14, and the discrepancy in results is assumed to be due to a simple mislabeling of either the modes or coefficients.

Our next aspect of verification was the testing of the decomposition technique itself. This followed along the same lines as the methods used in Tumin's 2006[16] and 2007[17] outlines, whereby signals were composed by summing several different eigenfunctions of both the discrete and continuous spectra with various weights. This composite signal is then decomposed in an attempt to recover the known weights used in its construction.

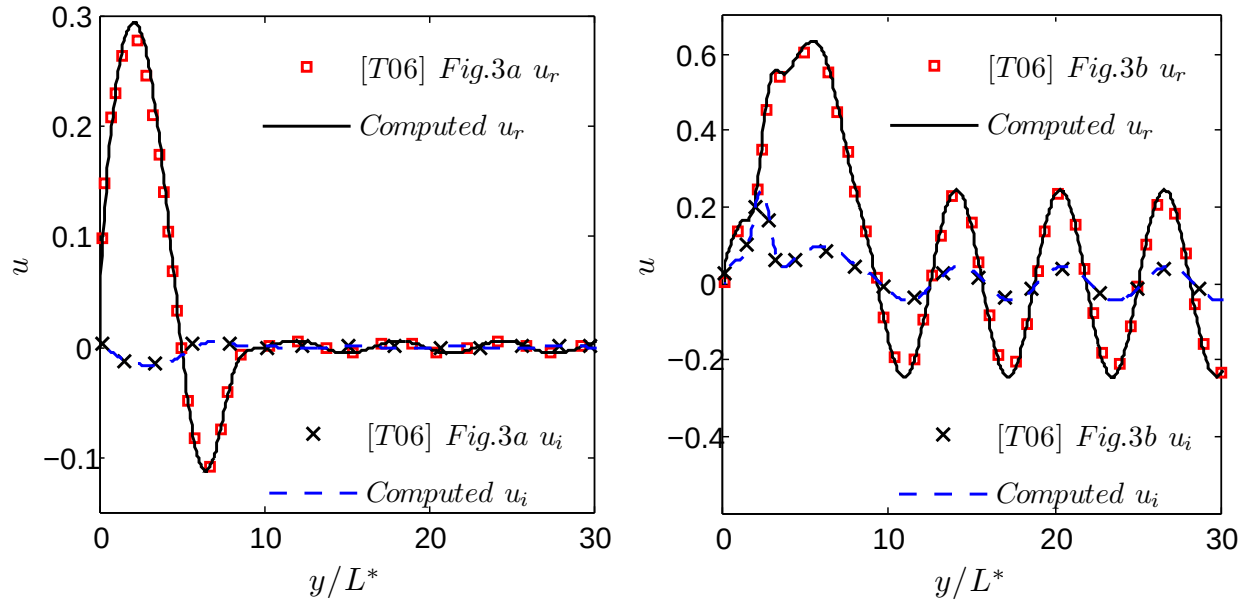

(a) (b)

Figure 10: Comparisons of continuous vorticity mode A (a) and continuous entropy mode (b) from Fig. 2 of reference T06[16] to computed values, $M = 5.95,\ T_w/T_{ad} = 0.1,\ F = 10^{-4},\ Re = 1500,\ \beta = 0.16,\ k = 1.$

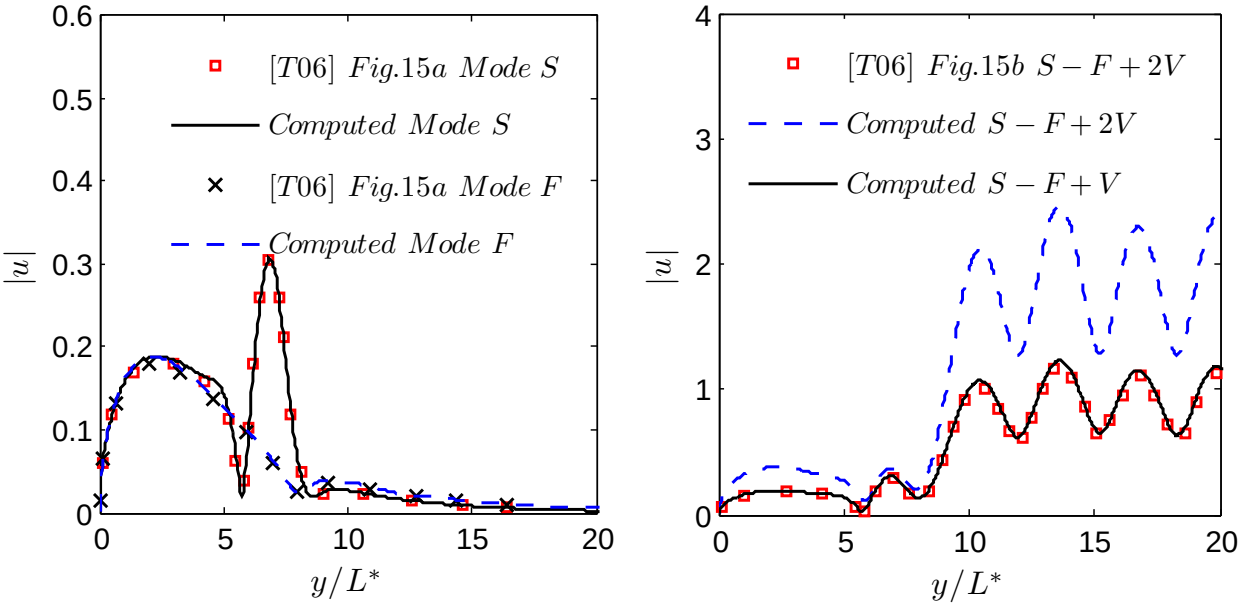

(a) (b)

Figure 11: Comparisons of discrete modes (a) and discrete and continuous vorticity mode sum (b) from Fig. 15 in reference T06[16] to computed values, $M = 5.95,\ T_w/T_{ad} = 0.1,\ F = 10^{-4},\ Re = 1895,\ \beta = 0.16,\ k = 1.$

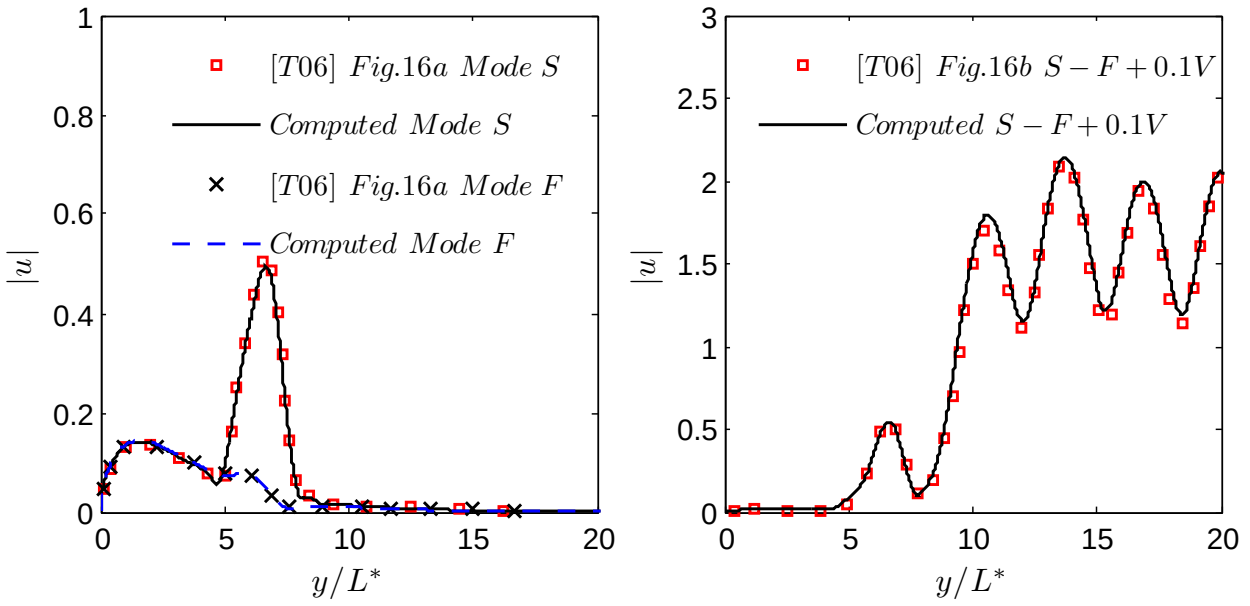

(a) (b)

Figure 12: Comparisons of discrete modes (a) and discrete and continuous vorticity mode sum (b) from Fig. 16 in reference T06[16] to computed values, $M = 5.95,\ T_w/T_{ad} = 0.1,\ F = 10^{-4},\ Re = 2300,\ \beta = 0.16,\ k = 1$.

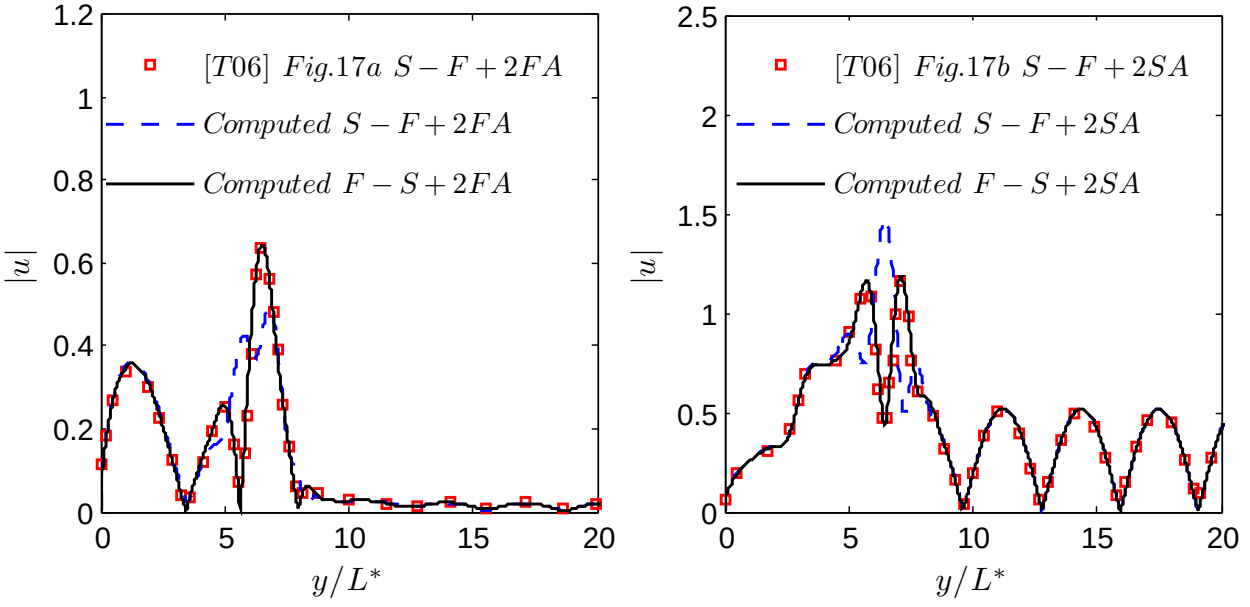

(a) (b)

Figure 13: Comparisons of discrete and continuous fast acoustic mode sum (a) and discrete and continuous slow acoustic mode sum (b) from Fig. 17 in reference T06[16] to computed values, $M = 5.95,\ T_w/T_{ad} = 0.1,\ F = 10^{-4},\ Re = 2300,\ \beta = 0.16,\ k = 1$.

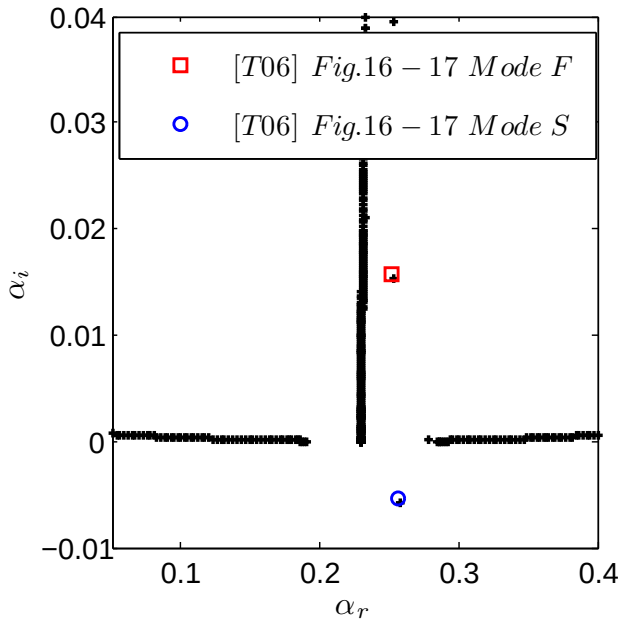

Figure 14: Global eigenvalue spectrum and local eigenvalue search results for the conditions specified in Fig. 12 and 13, $M = 5.95,\ T_w/T_{ad} = 0.1,\ F = 10^{-4},\ Re = 2300,\ \beta = 0.16$.

We begin with the composite signals that have already been constructed in our previous figures. In Figure 11b, we have a flow over a flat plate with the properties $M = 5.95,\ T_w/T_{ad} = 0.1,\ F = 10^{-4},\ Re = 1895,\ \beta = 0.16$, and $k = 1$. For this figure the coefficients used are $C_S = 1,\ C_F = -1$, and $C_V = 1$, where we again note that we have assumed a different value of C_V than that claimed in the source. Decomposing this composite signal using the method outlined in Section III D recovers the coefficients: $C_S = 1.00014 + i3.82155 \times 10^{-5}$ and $C_F = -1.00089 - i1.50343 \times 10^{-4}$.

For Figures 13a and 13b, we have flow over a flat plate with the properties $M = 5.95,\ T_w/T_{ad} = 0.1,\ F = 10^{-4},\ Re = 2300,\ \beta = 0.16$,and $k = 1$. Figure 13a constructs a composite signal using the two discrete modes and a weighted fast acoustic continuous mode, while Figure 13b constructs a composite signal using the two discrete modes and a weighted slow acoustic continuous mode. The exact coefficients for the composite signal in the two cases are $C_F = 1,\ C_S = -1,\ C_{FA} = 2$ and $C_F = 1,\ C_S = -1,\ C_{SA} = 2$ respectively. Upon performing the decomposition, the recovered discrete coefficients for the first case are $C_F = 1.00035 - i4.28462 \times 10^{-5}$ and $C_S = -1.00001 + i1.14985 \times 10^{-4}$. For the second case, the coefficients are determined as $C_F = 0.99679 + i1.95036 \times 10^{-3}$ and $C_S = -0.99911 - i7.13535 \times 10^{-4}$.

In Figure 15, a signal is constructed using the two discrete modes, mode F and mode S, and also two continuous modes, one fast acoustic (FA) and one slow acoustic (SA). The flow conditions for this case are the same as those specified for Figure 11b, $M = 5.95,\ T_w/T_{ad} = 0.1,\ F = 10^{-4},\ Re = 1895,\ \beta = 0.16$,and $k = 1$, however, with coefficients $C_F = -1,\ C_S = 1,\ C_{FA} = 2$, and $C_{SA} = 0.1$. Performing the decomposition, we recover coefficients for the discrete modes, $C_F = -0.999944 - i2.25455 \times 10^{-4},\ C_S = 1.00006 + i6.91611 \times 10^{-5}$. In the figure, the re-composed signal, including both the discrete and continuous modes, is plotted against the original as an indicator of the total error of the process.

Some level of verification was also performed for the specific case to be analyzed, that is, the DNS data for the hotspot perturbation on a flared cone. Using the meanflow from various stations, the mode F and mode S eigensolutions were characterized by applying the fundamental solution superposition technique to this data. A comparison of these results was made to the LST results described in Huang and Zhong's 2014 paper.[14] The comparisons are illustrated in Figure 16a with the neutral stability frequency/locations for both branches of Mode S, and in Figures 16b and 17 where the non-dimensional phase speed, non-dimensional wave number, and growth rate are shown for both discrete modes. The definitions for the terms in the plots are briefly recapitulated:

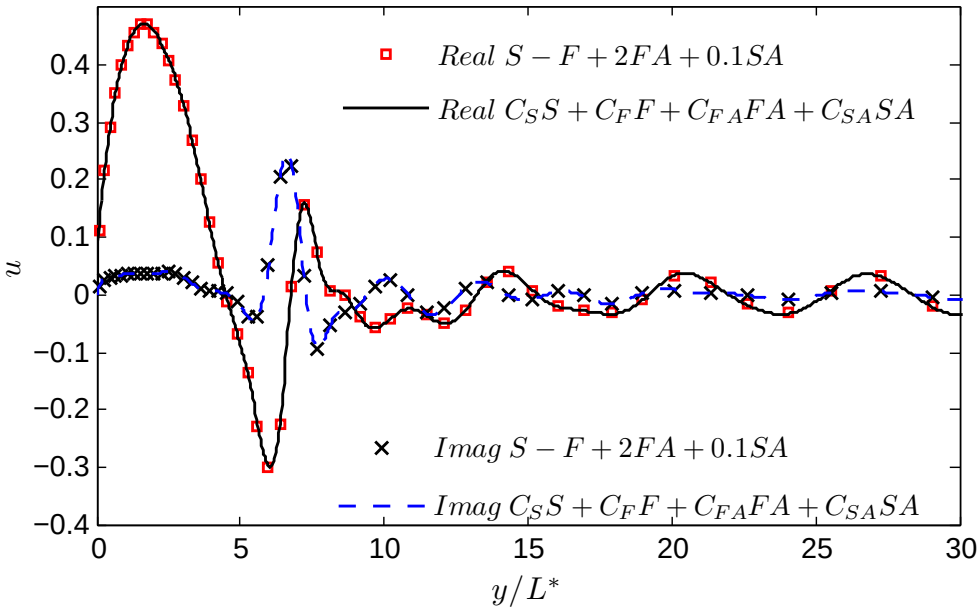

Figure 15: Comparison of exact signal and recomposed signal, $C_S = 1$, $C_F = -1$, $C_{FA} = 2$, $C_{SA} = 0.1$, $M = 5.95$, $T_w/T_{ad} = 0.1$, $F = 10^{-4}$, $Re = 1895$, $\beta = 0.16$, $k = 1$.

$$Non - dimensional\ Phase\ Speed = \frac{\omega}{\alpha_r} \tag{51}$$

$$Non - dimensional\ Wave\ Number = \alpha_r \tag{52}$$

$$Dimensional\ Growth\ Rate = \frac{-\alpha_i}{L^*} \tag{53}$$

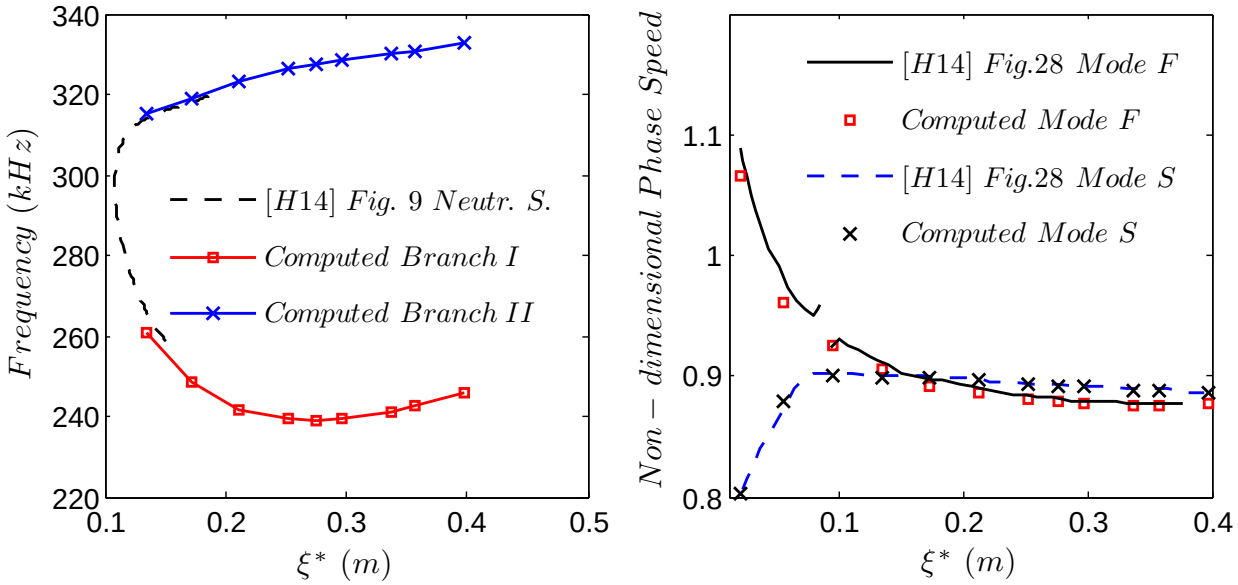

(a) (b)

Figure 16: Comparison of Mode S neutral stability curve (a) and non-dimensional phase speed for $f \approx 293\ kHz$ (b) from Huang & Zhong's 2014 analysis[14] to computed values.

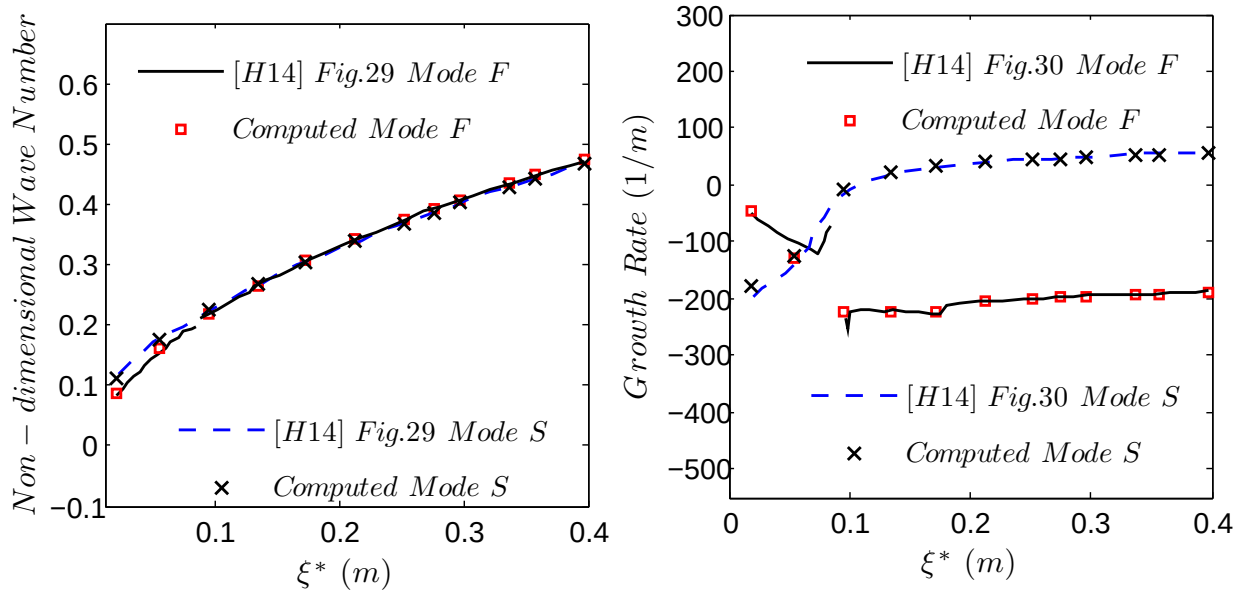

(a) (b)

Figure 17: Comparison of $f \approx 293\ kHz$ non-dimensional wave number (a) and dimensional growth rate (b) from Huang & Zhong's 2014 analysis[14] to computed values.

V. Simulation Results and Analysis

For the DNS analysis, the regions of consideration were discretized with a computational grid, a portion of which is shown in Figure 4. Due to the limited computational power available, the simulation was divided into 21 zones, with zone 1 encompassing the cone's hemispherical nose and zones 2 through 21 proceeding downstream and along the compression walls of the cone. As the data sets arising from DNS computations can be vast, the data was only saved at the entrance of each zone and the analysis to follow was limited to these locations. For more information about the DNS computations, the reader is referred to the source.[11]

A. Qualitative Receptivity Analysis

The wall pressure perturbation evolution on the compression cone is recorded in time at various spatial locations in the downstream direction. Figure 18 and Figure 19 plot the time-history traces, where the wall pressure perturbation amplitude is given relative to the freestream pressure. In Figure 18, one may note that the perturbation time-history profile begins with a relatively monotonic shape consisting of a main peak and a lower peak. It was concluded in Huang & Zhong's 2014 analysis[14] that these are likely fast acoustic and slow acoustic waves, which gradually decay as they travel downstream - eventually splitting into multiple peaks. It was further suggested that this may be due to the energy shift from one wave mode to another, caused by viscous effects within the boundary layer. In Figure 19, the multiple peaks in the perturbation begin to split into two distinct components - one with more a oscillatory profile and another that is comparatively smooth. As these perturbations travel further downstream, it is seen that the amplitudes decay and the two components depart from each other. In this analysis, it was determined that these two elements constitute separate wave modes, with distinct perturbation profiles and group velocities. Moving further downstream, another new perturbation mode appears that quickly grows to become the dominant instability in the boundary layer. This new mode, appearing in the time-history profile around $x^* = 0.25m$, was attributed in the previous LST analysis to the mode S instability.

Applying the Fourier transform method described in Section II C permits transition of the analysis from the temporal domain to the frequency domain. This transformation, also performed in the previous work, is given by Figure 20, which demonstrates the spectrum of pressure perturbations on the wall over a range of frequencies and streamwise locations. We note the logarithmic scaling of the plot, and the clearly demonstrated spatially growing peak within the approximately 260 kHz to 320 kHz frequency range. By contrast, the peak to the left of this range, at approximately 190 kHz to 260 kHz, appears to be decaying spatially and was attributed to the stable mode F perturbation. In the prior analysis,[14] the DNS data downstream was considered in the downstream regions where the perturbation is clearly dominated by the 260-320 kHz frequency peak. By comparing the DNS values of growth rate, mode shapes, wave speed, phase velocity, etc., it was determined that in these regions, the flow was indeed mode S dominant. It was postulated that the full mechanism by which receptivity proceeds for this problem is the initial excitement of mode F by incoming acoustic waves, followed by the later stimulation of mode S in the vicinity of the synchronization point via the intermodal exchange mechanism discussed by Fedorov and Khokhlov.[27] The full analysis is available in the reference works,[13,14] with more information on the methods used available therein.

A peculiarity of the analysis to follow is noted in Figure 20, where the reader may note the frequencies considered. The range of the spectral analysis consists of the frequencies 100 kHz to 600 kHz, generally encompassing the regions considered in the prior works. The exceptions to this are the three upstream locations, $\xi^* = 0.019m$, $\xi^* = 0.055m$, and $\xi^* = 0.094m$ where, for these locations, the analysis is instead limited to the 100 kHz and 300 kHz frequency range. The discrepancy arises from the method of storing DNS data, with the first 10 zones storing the sum of meanflow and perturbation quantities, and with the later zones separating these values. When the perturbation values become small - as they do for frequencies greater than ∼300 kHz at $\xi^* = 0.094m$ - the difference in scale between the meanflow quantities and the perturbed quantities becomes so vast as to induce significant numerical error in the isolation of the perturbation values. This error makes analysis of these frequencies prohibitive without re-computation of the zones in question, and so we note the region of analysis for these zones is truncated for the purposes of this paper.

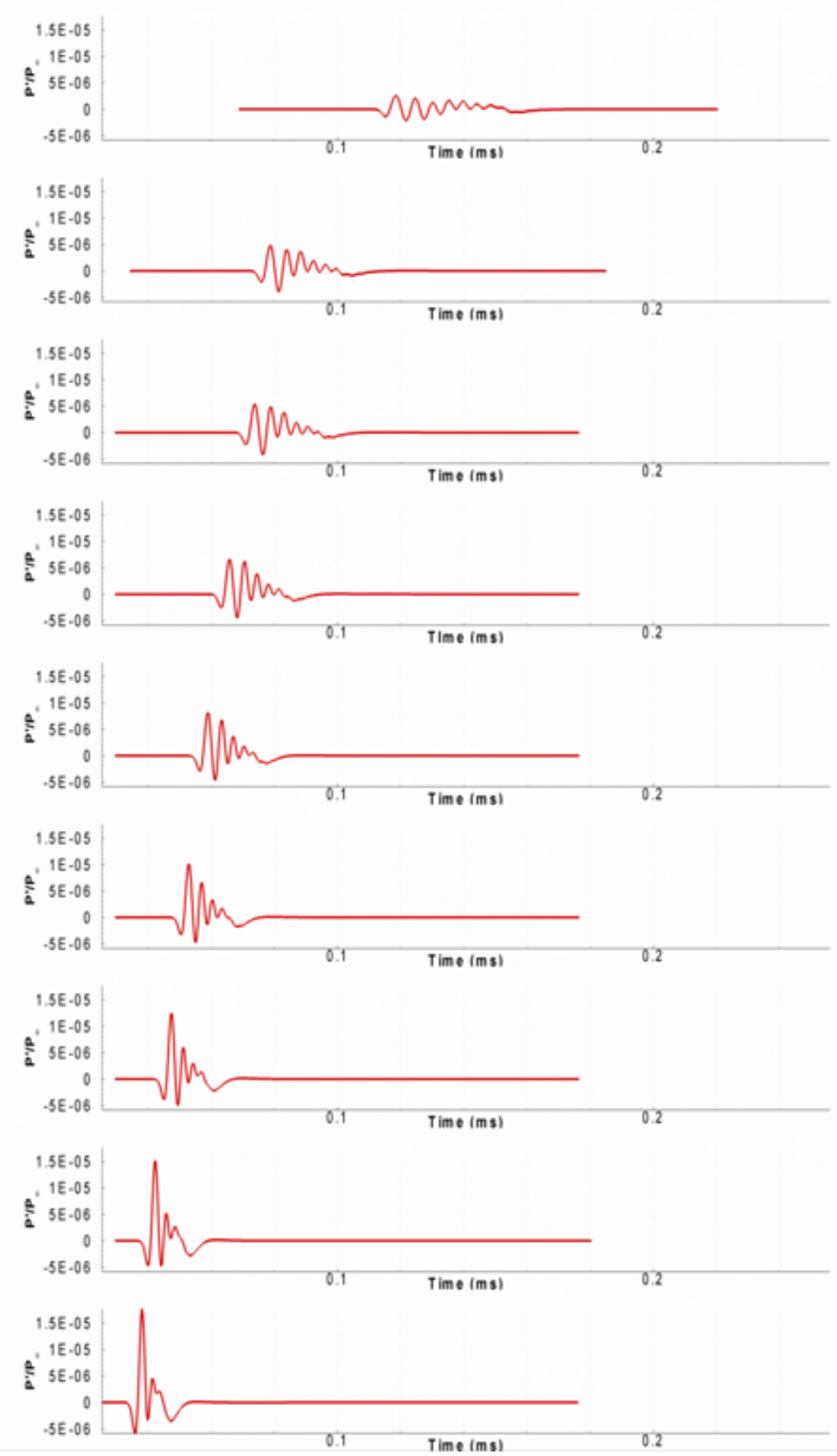

Figure 18: Time-history traces of pressure wall-perturbation at various streamwise locations on the upstream portion of the cone.

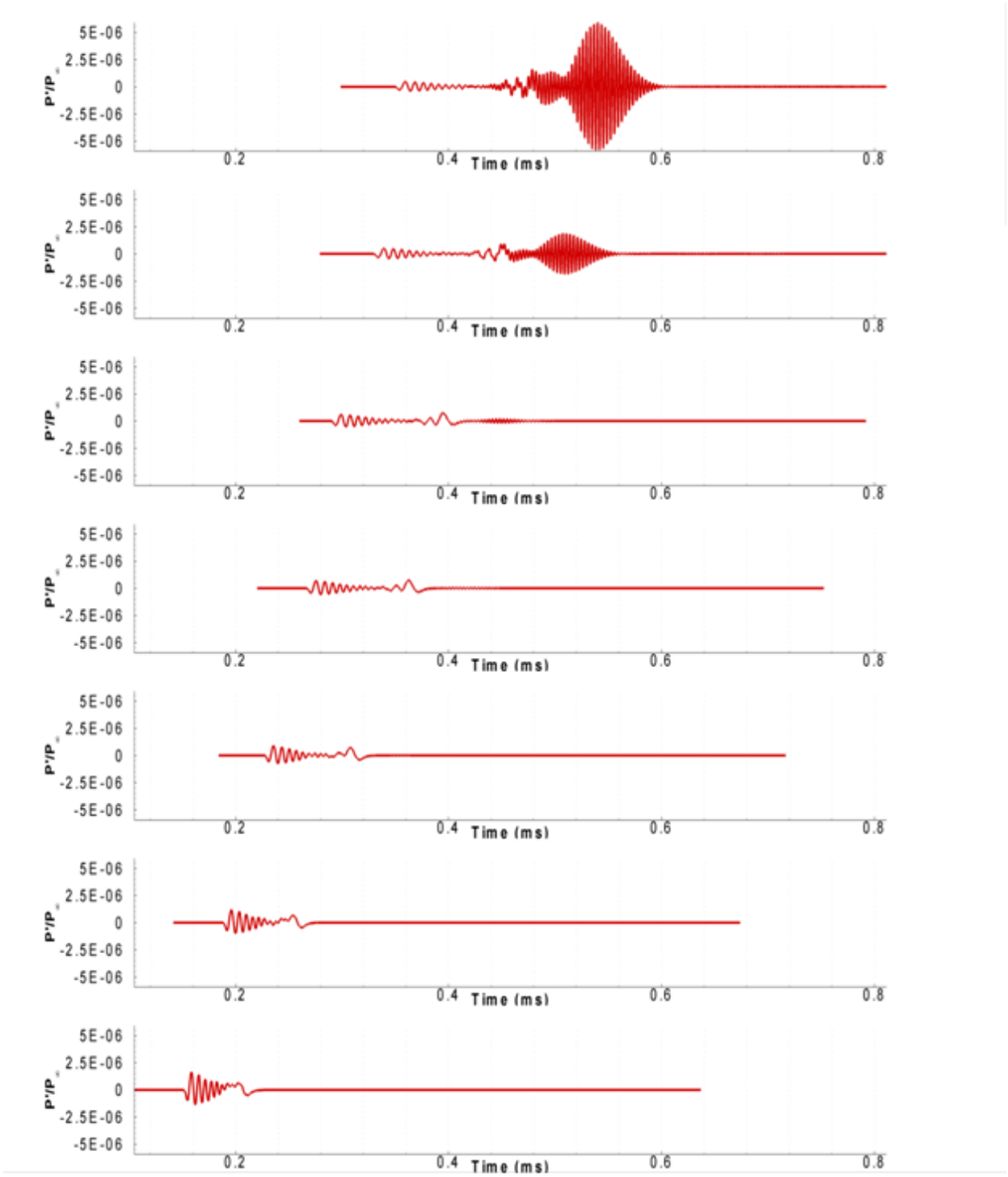

Figure 19: Time-history traces of pressure wall-perturbation at various streamwise locations on the downstream portion of the cone.

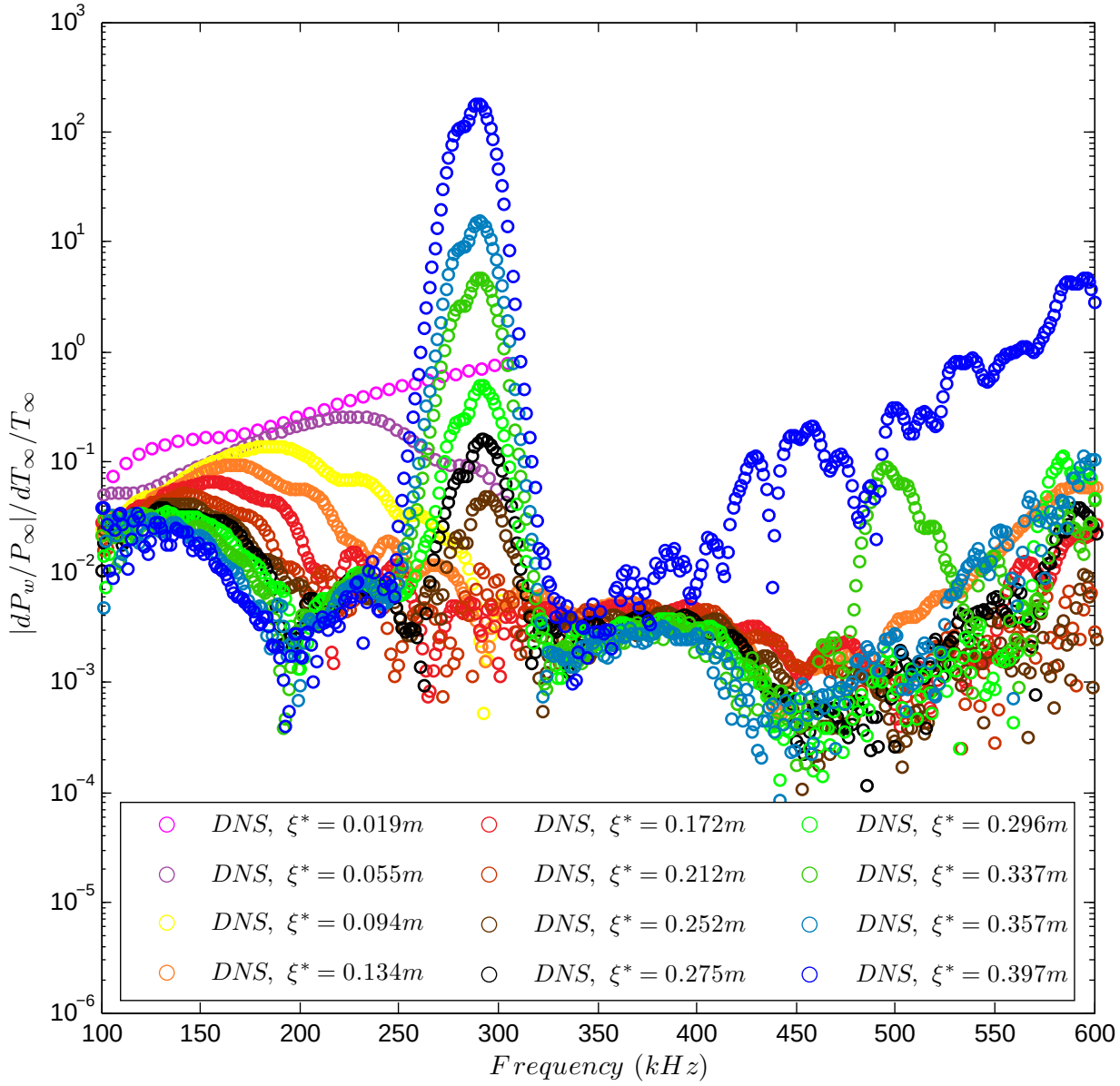

Figure 20: Wall pressure perturbations from DNS/FFT at various locations and frequencies normalized by the freestream temperature perturbation.

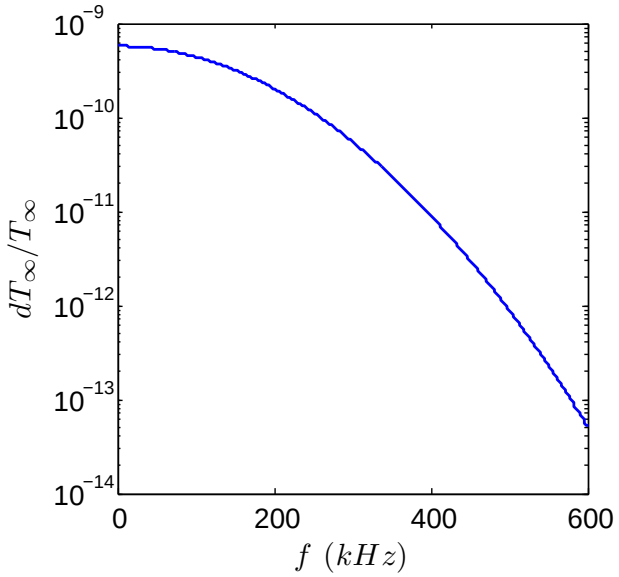

Figure 21: Freestream temperature perturbation of the hot spot, transformed to the frequency domain.

B. Theoretical Receptivity Analysis

With the multimode decomposition implementation verified against previous results, the method was then applied to the DNS data via the procedure outlined in Section III. The DNS data at each point along the cone consisted of the meanflow data and perturbation data in the wall-normal direction across the shock-fitting domain. The perturbation data, consisting of the time history of the perturbed flow, was transformed into the individual frequencies of the wave packet using the Fourier transform method as described in Section II C. For each frequency, the multimode decomposition could then be performed as specified in Section III D and the coefficients calculated.

As outlined above, with the previous analysis it was only possible to make qualitative assessments of the behavior of the DNS perturbation values by utilizing comparisons to LST modes to assess the prevalence of instabilities. In the present analysis, however, we can determine the local coefficient amplitudes of each mode for different frequencies and locations along the cone - thus performing an analysis of the data that is more anchored in the problem's theoretical background.

The decomposition was performed primarily for the two discrete modes F and S, with the results shown in Figures 22-34 illustrating the data determined from these decompositions. The y-value in Figures 22-24 represents the ratio between the two terms:

$$\frac{|dP_{wall}/P_\infty|}{dT_\infty/T_\infty} \tag{54}$$

The term in the numerator is the magnitude of the perturbation pressure at the wall, non-dimensionalized by the freestream pressure. The term in the denominator is the freestream temperature perturbation - that is, the hotspot temperature - normalized by the freestream meanflow temperature. As shown in Figure 21, the hotspot perturbation has an amplitude that varies by frequency, and is not constant across the frequency spectrum. To account for this, the perturbation values for both the response, dP_{wall}, and the freestream forcing, dT_∞, are separated into their component values for each frequency and compared only to their corresponding values at the same frequency. The frequency range thus forms the x-axis in Figures 22-24, while the terms given by the y-axis provide a reference ratio of the boundary layer's response relative to the initial input. These are values which we generally term the "receptivity coefficients" for the problem:

$$C_{recpt} = \frac{|dP_{wall}/P_\infty|}{dT_\infty/T_\infty} \tag{55}$$

Figure 20, therefore, shows these values exactly as they arise from the DNS results, with the total response of the system related to the initial perturbation, across the range of many frequencies and at several locations along the cone. In our new analysis, we take the DNS data given by Figure 20 and apply the decomposition of Section III D to determine the contribution of each boundary layer mode. These results are presented in Figures 22 and 23, showing the decomposition into mode F and mode S respectively. The coefficients determined for each mode are given by lines, while the markers indicate the full DNS data transformed to the frequency-spectrum for each location.

1. Discrete Modes

The results of the previous LST analysis are largely confirmed, with each peak matching their expected mode. The low frequency peak of the DNS data in the region of $\sim 120\ kHz$ to $\sim 240\ kHz$ matches that of the decomposed mode F result very closely. By comparison, in this frequency range the mode S coefficients are generally about one order of magnitude smaller, with the overall perturbation therefore dominated by mode F in the upstream regions. Both modes are observed to be decaying relatively steadily as they travel downstream over this frequency range, tending to indicate an initial excitation of both modes in the frequency range in which the freestream perturbations are strongest.

Similarly, as the perturbation signal moves downstream, both mode F and mode S are excited in the vicinity of the $\sim 240\ kHz$ to $\sim 320\ kHz$ peak, suggesting interaction between the modes. In this frequency range, the mode S coefficients are initially excited but decaying in the upstream regions, and at approximately $\xi^* = 0.134m$, these values appear to reach a minimum. For locations downstream of this, beginning with $\xi^* = 0.172m$, the peak in the mode S coefficients begins to take shape and quickly grow. This location corresponds to the first station analyzed that is downstream of the synchronization point for the most unstable frequency, $\sim 293\ kHz$. The exact location of the synchronization point for this frequency is given as approximately $\xi^* = 0.16m$.[14] Thus, the observed excitation of this frequency at that location is significant, and indicative of the intermodal exchange suggested during the previous analysis. Although both modes are excited in this frequency range, the decomposed mode F coefficients are still several orders of magnitude smaller than the DNS peak values, while the mode S results are quite comparable. As expected, our results thus indicate the flow is given to mode S dominance due to a growing perturbation in the ~ 240 to $\sim 320\ kHz$ frequency range that begins at or near the $\sim 293\ kHz$ synchronization point.

An interesting result not captured by the previous analysis is the high frequency mode F peak in the region furthest downstream. Although the flow is still mode S dominant in this region, the amplitude of this high frequency mode F regime appears larger even than that of the upstream, low frequency peak. We do reiterate, however, that the coefficient plotted is relative to the freestream temperature perturbation, which decreases in value significantly at higher frequencies. Thus, the high frequency mode F peak is only indicative of large perturbations in the high frequency regime relative to the inputs at the same frequency from the freestream. It is further noted that at these high frequencies, a third discrete mode was observed to emerge from the continuous fast acoustic spectrum. Although decomposition was not performed for this accessory mode, the link, if any, between these high frequency phenomena as they relate to the problem at hand may bear further investigation.

Figure 24 compares the sum of both the mode F and mode S contributions to the DNS data at each frequency and location. The close match between the mode sum and the DNS data indicates that the vast majority of the contribution to the results within the boundary layer arise due to the influence of these two modes. The continuous modes, by comparison, appear to have limited influence within the boundary layer, although this can not necessarily be said of the flow field in general.

2. Continuous Modes

Figures 25-26 demonstrate examples of continuous mode eigenfunctions at individual frequencies and locations along the cone. As is immediately apparent from the amplitudes of the eigenfunctions for different branches, the vorticity and entropy spectra experience strong decay as they penetrate the shock and boundary layer. As such, they provide very little contribution to the total observed result, with the main influences from the continuous spectrum being due to the fast and slow acoustic spectra. This finding is in line with the results of previous work that considered blowing/suction perturbations,[16,26] and found that the input of the vorticity and entropy modes were small relative to the acoustic modes.[18]

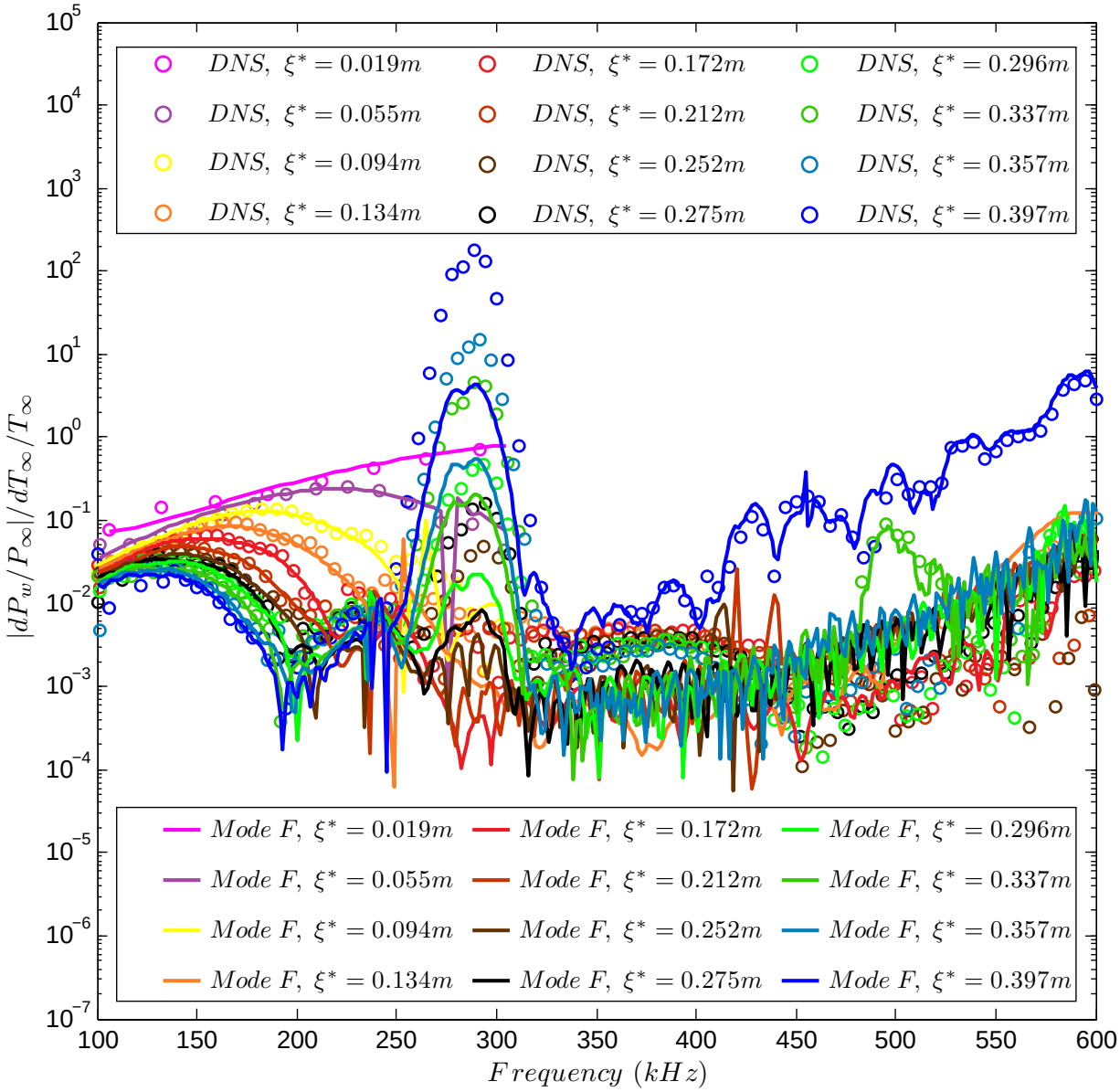

Figure 22: Magnitude of Mode F coefficients by frequency and location compared to DNS/FFT data.

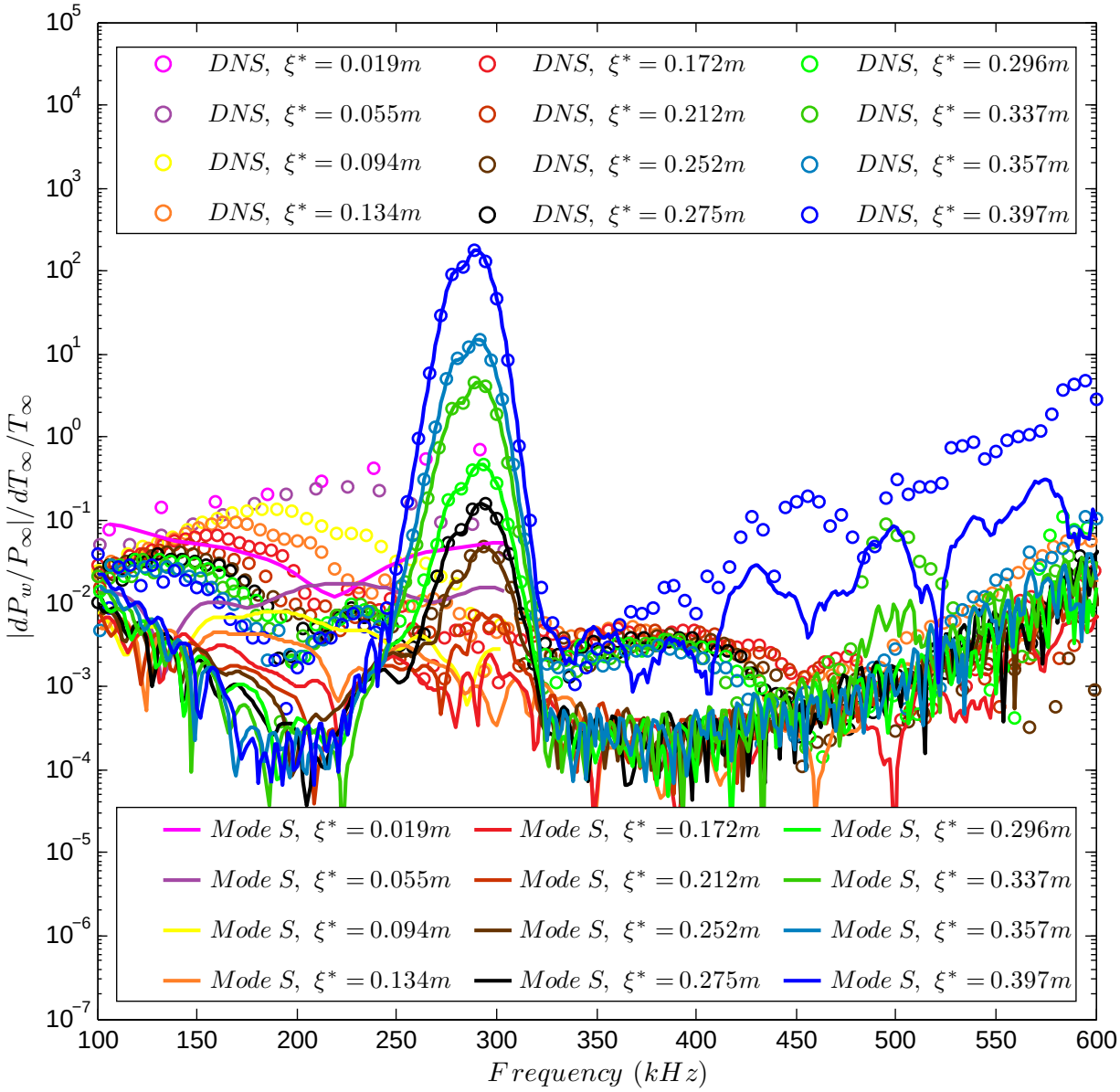

Figure 23: Magnitude of Mode S coefficients by frequency and location compared to DNS/FFT data.

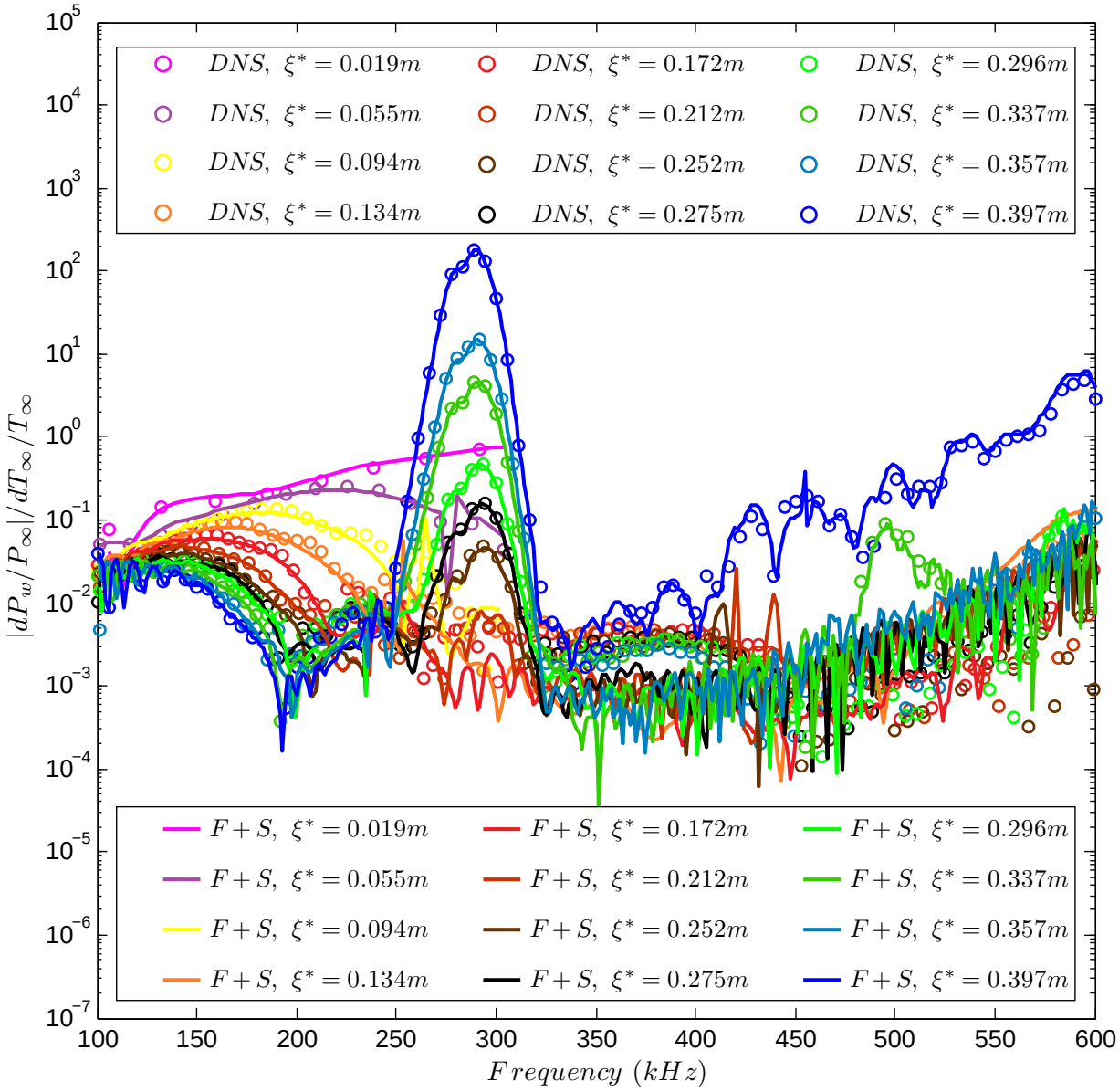

Figure 24: Magnitude of Mode F and Mode S coefficient sum by frequency and location compared to DNS/FFT data.

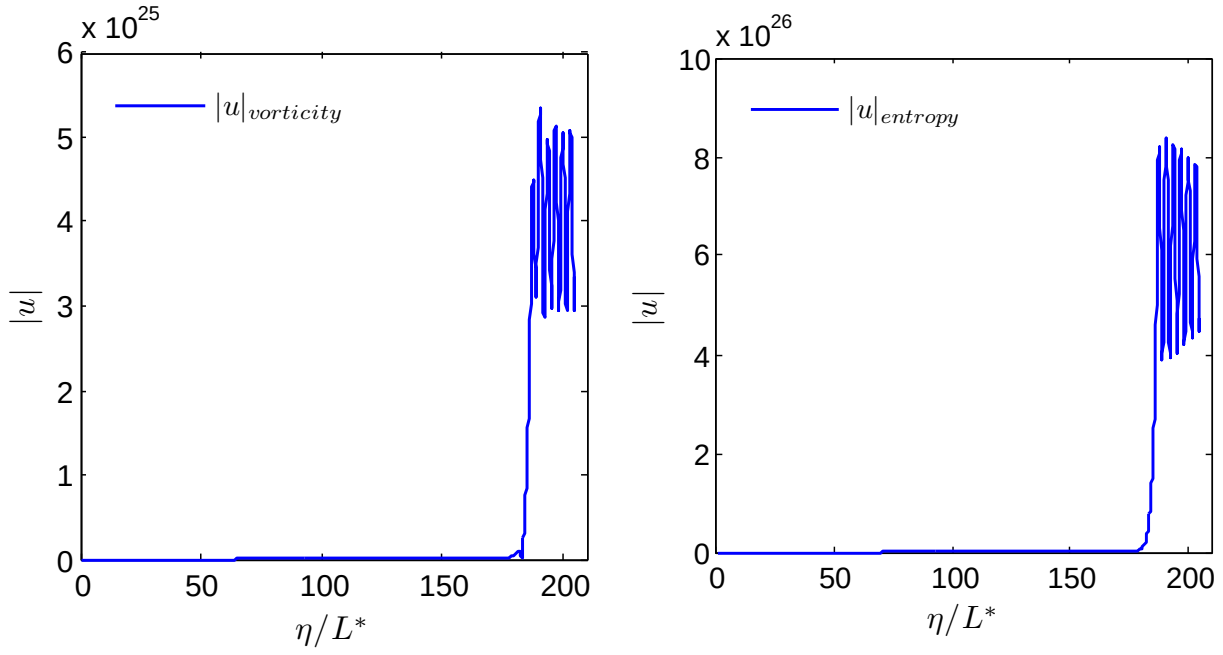

(a) (b)

Figure 25: Streamwise velocity eigenfunctions for vorticity A (a) and entropy (b) continuous modes at $\xi^* = 0.172m$, $f = 301\ kHz$, and $k = 1$.

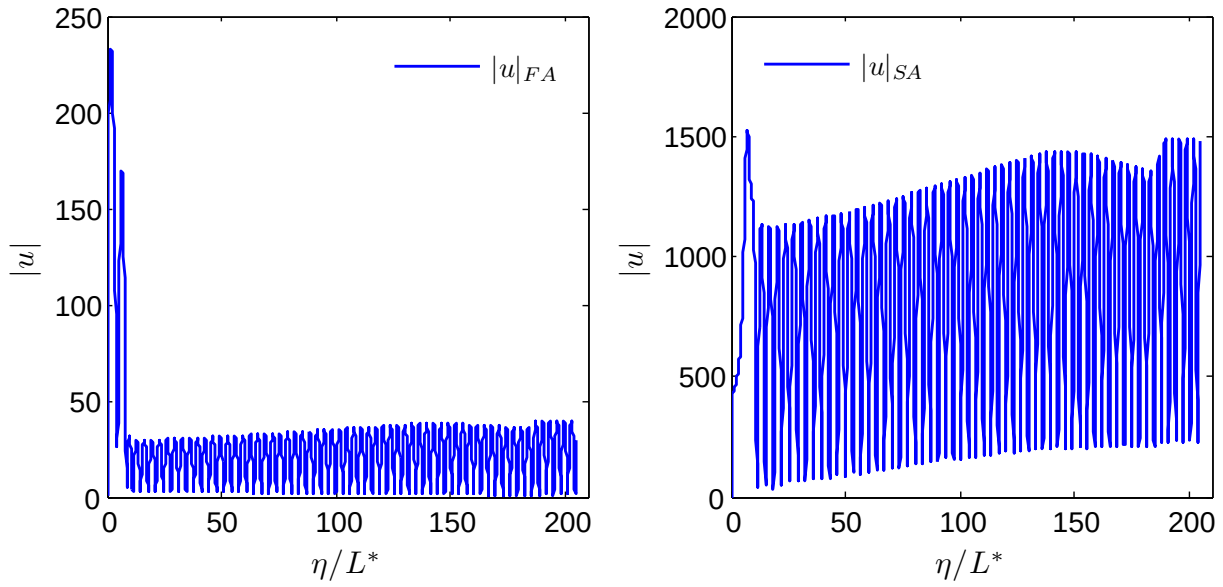

(a) (b)

Figure 26: Streamwise velocity eigenfunctions for fast acoustic (a) and slow acoustic (b) continuous modes at $\xi^* = 0.172m$, $f = 301\ kHz$, and $k = 1$.

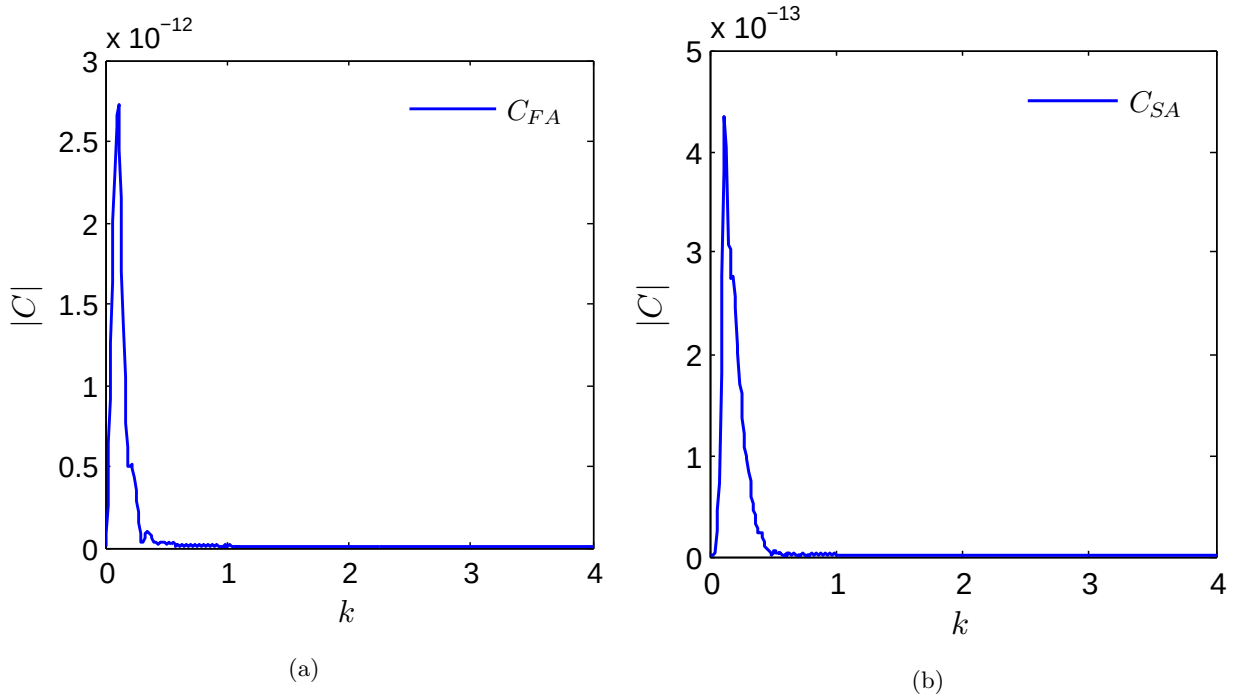

Figure 27: Continuous spectrum mode coefficient magnitudes for various k - fast acoustic (a) and slow acoustic (b) continuous modes at $\xi^* = 0.172m$ and $f = 100\ kHz$.

Decomposing the DNS data into components of the continuous spectrum requires discretization using the parameter k. In order to adequately resolve these spectra, a sufficiently fine stepping, Δk, is required, as well as a judicious choice of the range of k to analyze. As this typically involves the calculation of several hundred modes at each frequency and location of consideration, only a few such decompositions were performed to obtain a general picture of the influence of these mode types.

For the purpose of the continuous spectrum analysis, and in keeping with the finding above regarding the influence of the various continuous spectrum mode types, only the fast and slow acoustic branches were considered. For each location/frequency pair, the spectrum was discretized into 400 modes, with $0 \leq k \leq 4$. As with the discrete modes, the coefficient for each continuous spectrum mode is calculated with Equation 50. As shown in Figure 27, the continuous spectrum coefficients are generally largest for moderate values of k: $0 \lesssim k \lesssim 1$. In future work, it may be possible to achieve better accuracy and minimize the computations required by focusing on these values, perhaps through use of a stretched grid in k.

With the relevant continuous spectrum modes computed, it is then possible to construct a recomposed signal, comprising the elements of both the discrete and continuous spectra. These reconstructed modes are plotted in Figures 28-29, with locations and frequencies indicated. It is observed that although the fast and slow acoustic modes generally have marginal influence within the boundary layer, there is generally a comparatively large packet of acoustic waves located between the boundary layer and the shock. This is generally in line with the findings of the previous analyses[1,14] that indicated that the interaction of a hotspot and shock leads to the formation of fast and slow acoustic waves in the region behind the shock.

In addition to the fully recomposed modes, Figures 28-29 also indicate the components of the recomposed eigenfunctions that are attributable solely to the decaying boundary layer modes. As expected from our previous receptivity coefficient analysis, within the boundary layer the vast majority of the DNS perturbation is attributable to the sum of the mode F and mode S discrete modes. Outside of the boundary layer, however, there is generally a comparatively large packet of acoustic waves that exists in the region between the boundary layer and the shock. Of particular interest is the case shown in Figure 29b, representing a case far downstream at $s^* = 0.172m$ and localized within the frequency spectrum mode S peak, with $f = 301\ kHz$. For this case, we note that there still exists a continuous acoustic spectrum wave packet in the region outside the boundary layer, however, the magnitude of the mode S peak in this unstable, mode S

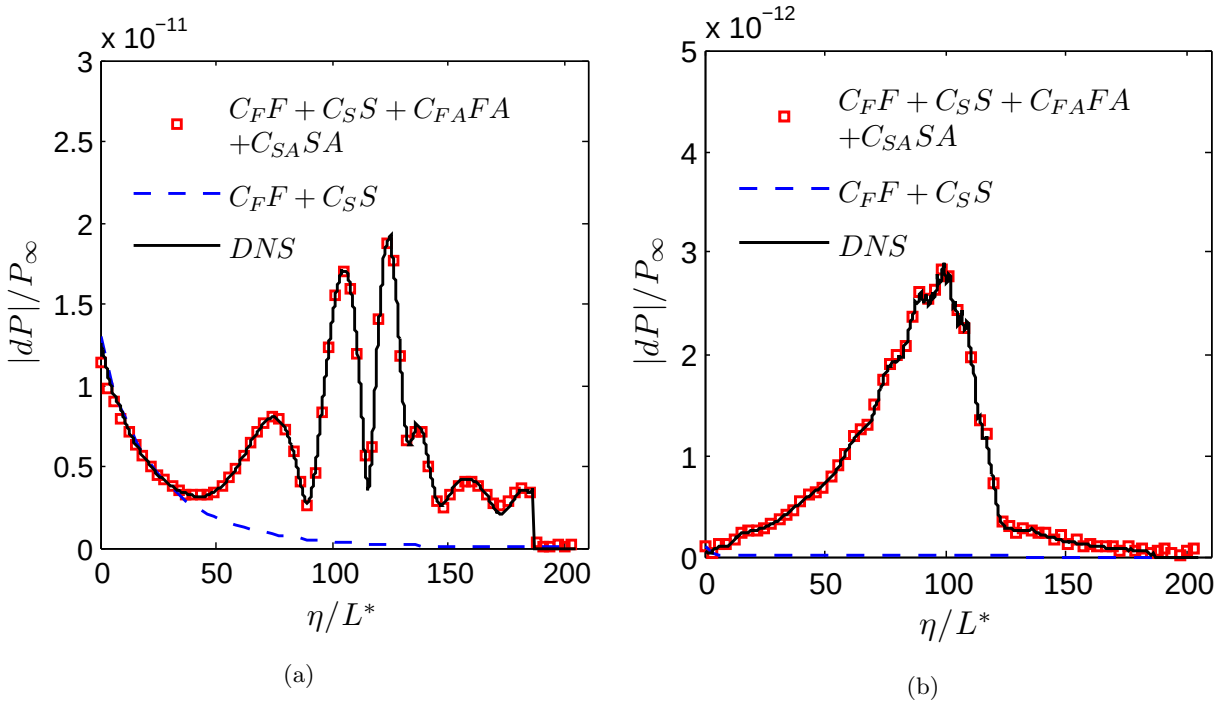

Figure 28: Comparison of DNS pressure data with recomposed sum of mode F, mode S, and fast and slow acoustic continuous modes at location $\xi^* = 0.172m$ for $f = 100\ kHz$ (a) and $f = 301\ kHz$ (b).

dominant location dwarfs the acoustic wave packet. This can be compared to Figure 28b, which represents the region just past the synchronization point where the mode S perturbation is just beginning to grow, and we note that the overall perturbation signal in this region is dominated by the acoustic waves external to the boundary layer. By contrast, Figure 28a and Figure 29a together demonstrate the evolution of the upstream, low frequency forcing in the boundary layer, with notable decay of the excitation within the boundary layer as these perturbations travel downstream. In the cases considered, we note that the inclusion of the two acoustic branches permits recomposition of the DNS eigenfunctions to a high level of accuracy.

We note another contribution of the continuous spectrum - the effect by which it influences mode F eigenfunctions. It is found that, in the vicinity of the mode F coalescence with the continuous vorticity/entropy spectrum, shown in Figure 30a, the eigenfunctions associated with mode F take on characteristics of the continuous spectrum. This is noted by the oscillatory nature of the discrete mode in the region near and outside of the boundary layer edge displayed in Figure 30b. Unlike the continuous spectrum modes, however, these values continue to decay as they oscillate, eventually going to zero to satisfy the boundary condition imposed on discrete modes. This finding is in line with the similar observation in the analysis conducted by Tumin, Wang, & Zhong in 2007,[18] and indicates that the existence of the continuous spectrum has an effect even on the discrete modes.

3. Receptivity Coefficients

In Figures 31-34, we present the same information given from Figures 22-23 in a clearer, though less precise format. In Figures 31 and 32, the decomposition of the DNS data into elements of mode F and S respectively are indicated by the color of the plot at that location and frequency. In Figures 33 and 34, we instead employ contours to indicate the range of data for each of the mode F and mode S decompositions. On each of the plots, we also include two lines which indicate the branch I and branch II neutral frequencies for each location. In both plots the branches indicate the mode S neutral frequencies at each location, with branch I corresponding to the lower frequency and branch II corresponding to the larger. This allows us to define the more typical receptivity coefficient,[28,29] the branch I receptivity coefficient:

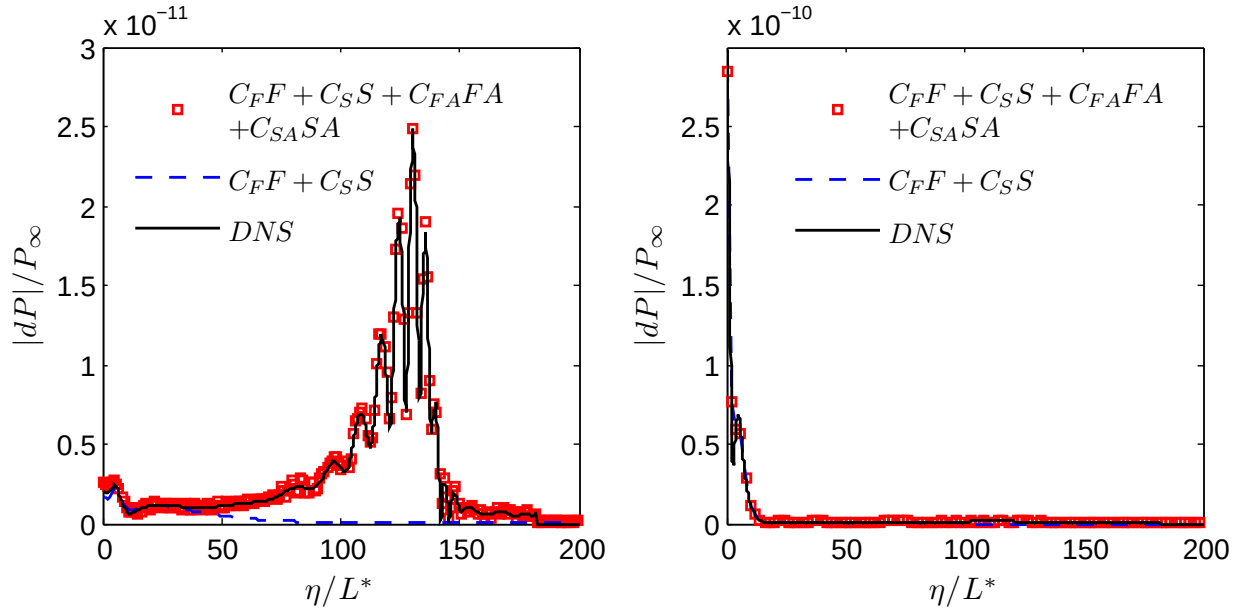

(a) (b)

Figure 29: Comparison of DNS pressure data with recomposed sum of mode F, mode S, and fast and slow acoustic continuous modes at location $\xi^* = 0.357m$ for $f = 101\ kHz$ (a) and $f = 300\ kHz$ (b).

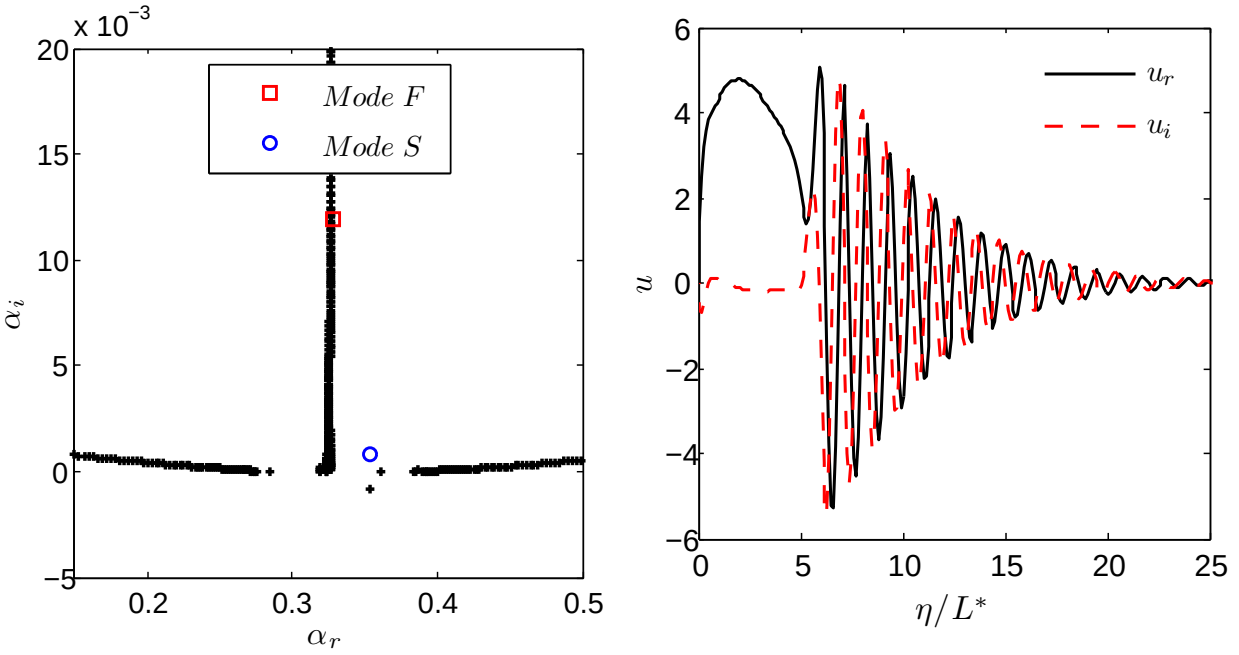

(a) (b)

Figure 30: Global eigenvalue spectrum (a) and mode F streamwise velocity eigenfunction at $\xi^* = 0.357m$ and $f = 238.5\ kHz$.

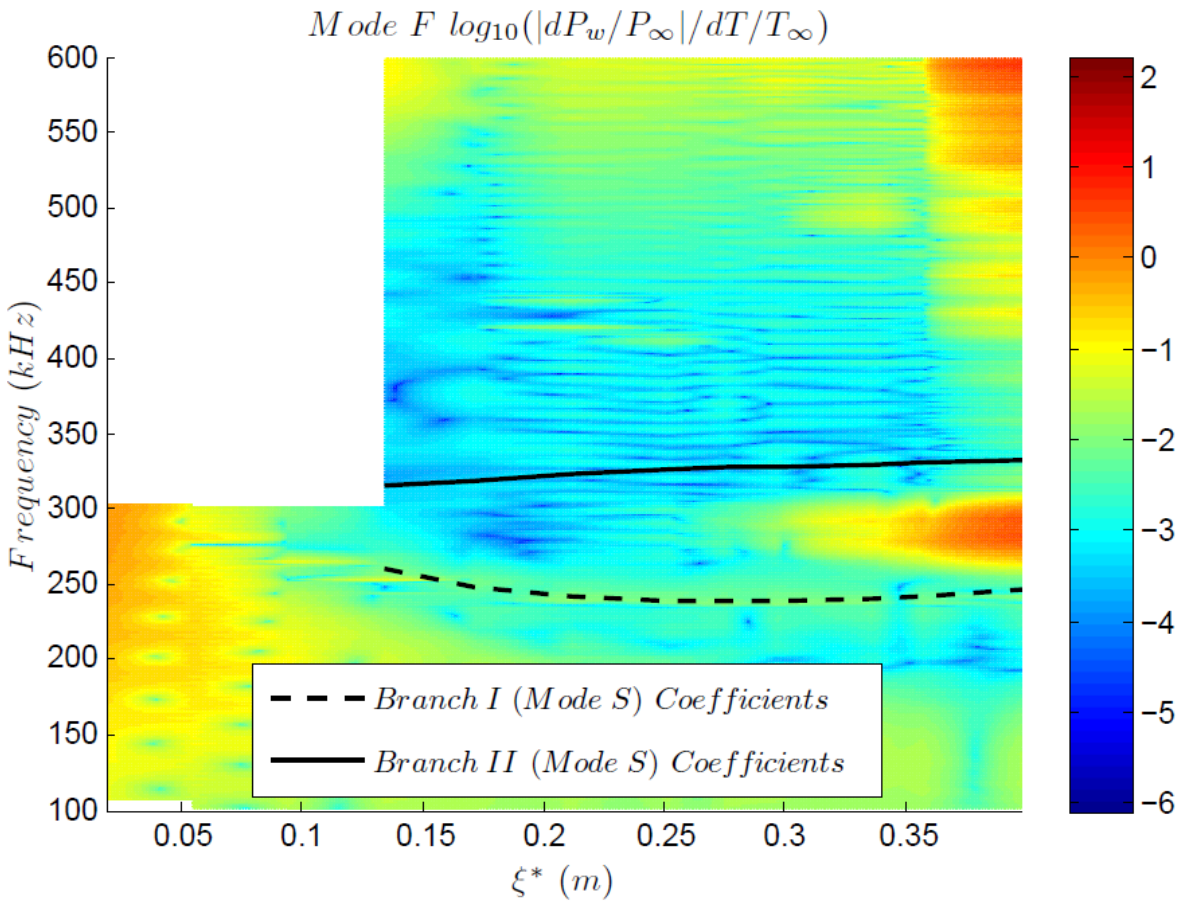

Figure 31: Magnitude of Mode F coefficients by location and frequency, with lines showing the branch I/II neutral stability frequencies/locations for Mode S

$$C_I = \frac{|dP_{wall}/P_\infty|_I}{dT_\infty/T_\infty} \tag{56}$$

where the subscript indicates that the pressure perturbation is evaluated at the branch I neutral point. The receptivity coefficients that characterize a system are typically given at frequencies/locations on the neutral stability curve, as perturbation amplitudes along the neutral stability curve represent the initial disturbance amplitudes. These can be contrasted with amplitudes at other frequencies/locations, which are attributable in part to spatial growth of the perturbation. The receptivity coefficients along the neutral stability curve thus give a truer picture of the basic response of the system to freestream forcing.

The values of these receptivity coefficients are then presented in figure 35, where results are given for both branch I and branch II neutral points. We see that, although the values are varying along the cone, there is a relatively dramatic increase in each for the furthest downstream location. The values are comparatively constant, however, taken in the context of the mode S pressure perturbation at the least stable frequency - which varies by location from $\sim 10^{-3}$ to $\sim 10^{2}$. The phase angles of the branch I and II receptivity coefficients, however, are difficult to discern any patterns from, with the angle typically changing by $> 180°$ from location to location. In future work, an analysis of additional locations along the cone may serve to better reveal the characteristic trend for these values.

In Balakumar & Kegerise's 2010 study,[28] receptivity coefficients were obtained for the same flared cone considered in our work, under identical freestream conditions. The receptivity coefficients determined therein were obtained via an e^N analysis facilitated by LST and PSE computations, and examined the cone's receptivity to acoustic waves. The frequency examined in that work was specified as $f = 292.5\ kHz$, and the

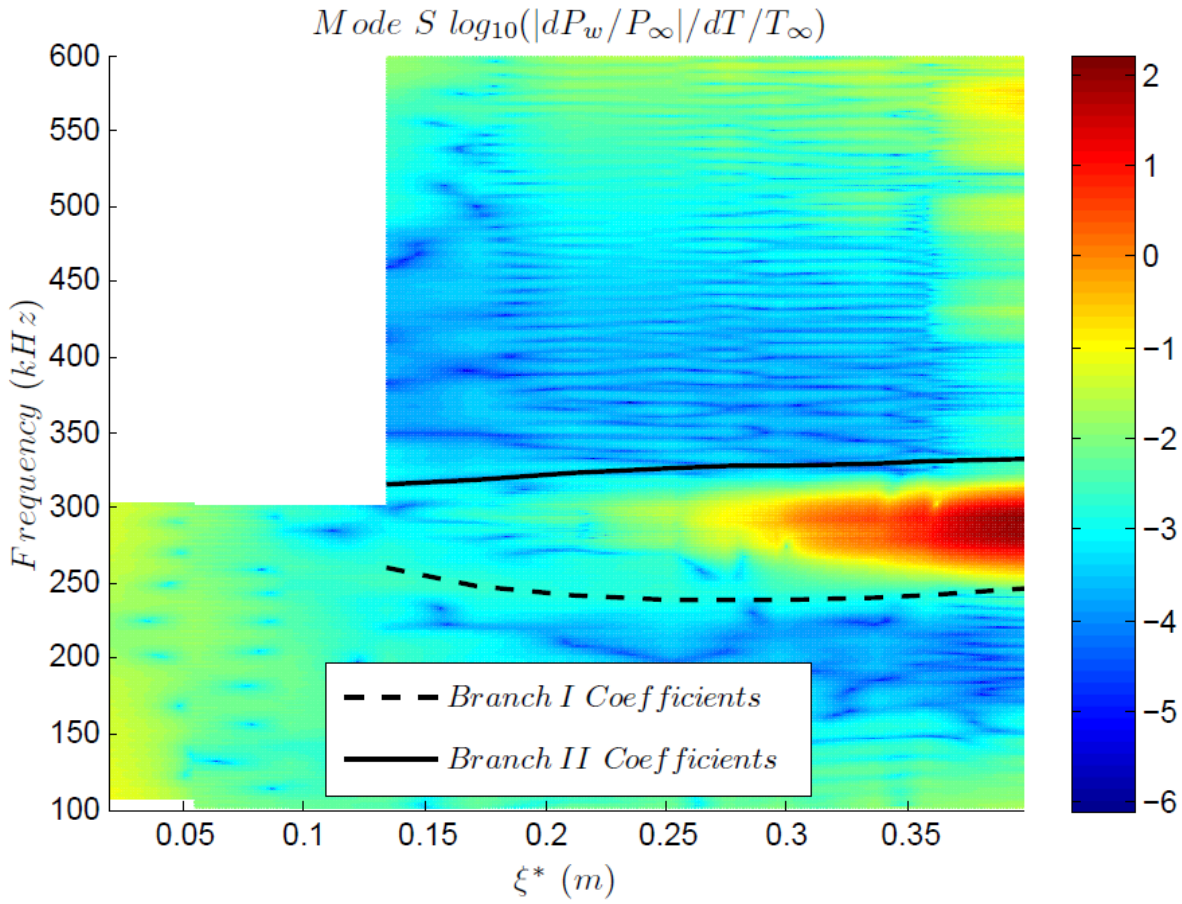

Figure 32: Magnitude of Mode S coefficients by location and frequency, with lines showing the branch I/II neutral stability frequencies/locations for Mode S.

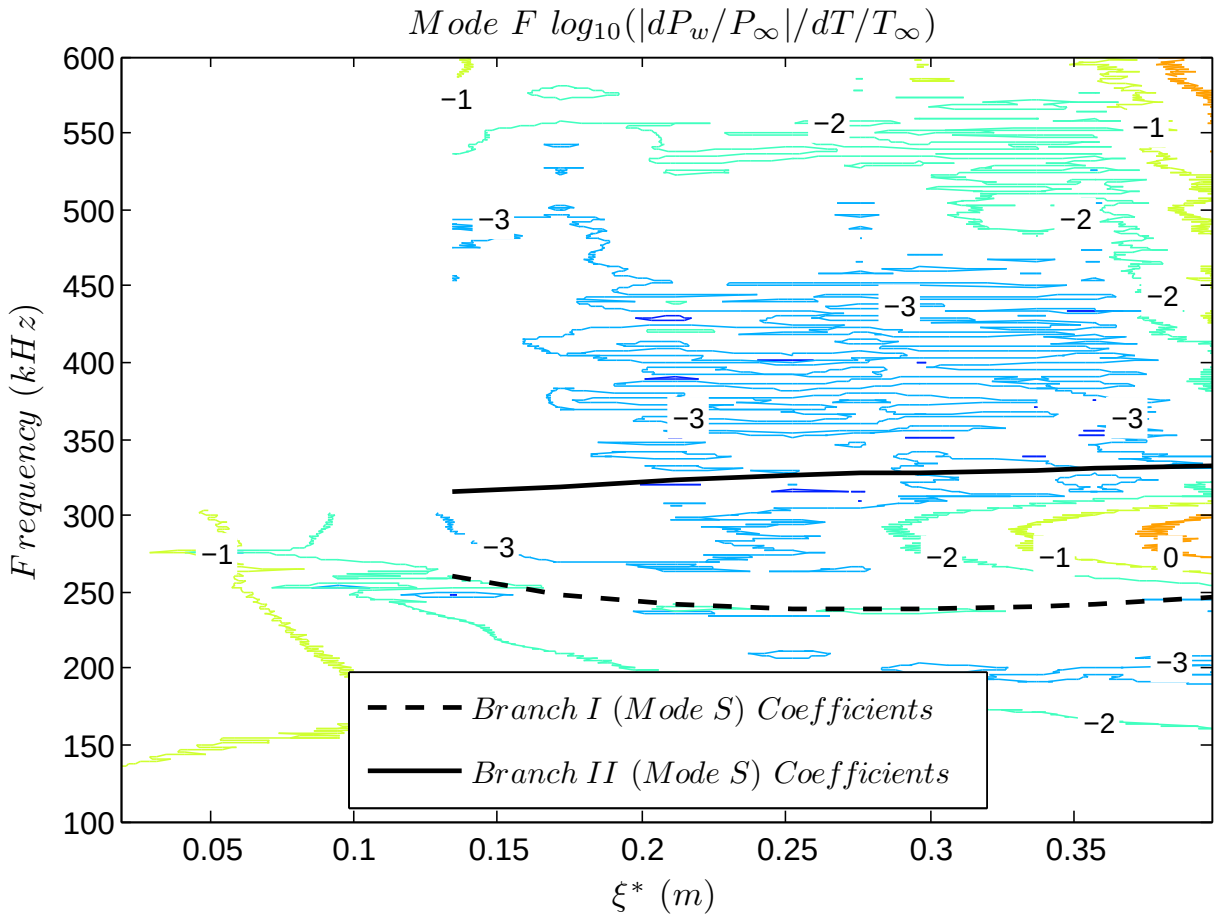

Figure 33: Magnitude of Mode F coefficients by location and frequency, with lines showing the branch I/II neutral stability frequencies/locations for Mode S.

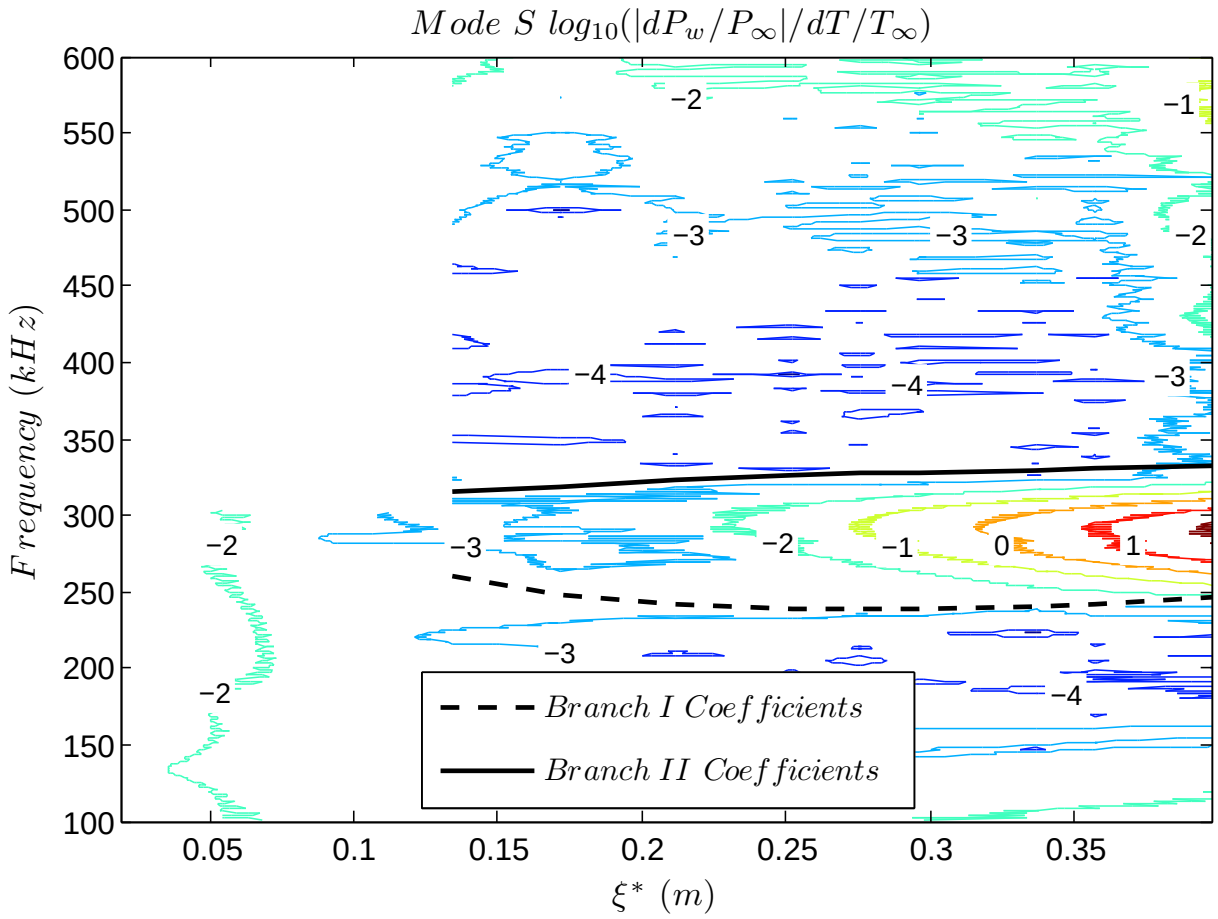

Figure 34: Magnitude of Mode S coefficients by location and frequency, with lines showing the branch I/II neutral stability frequencies/locations for Mode S.

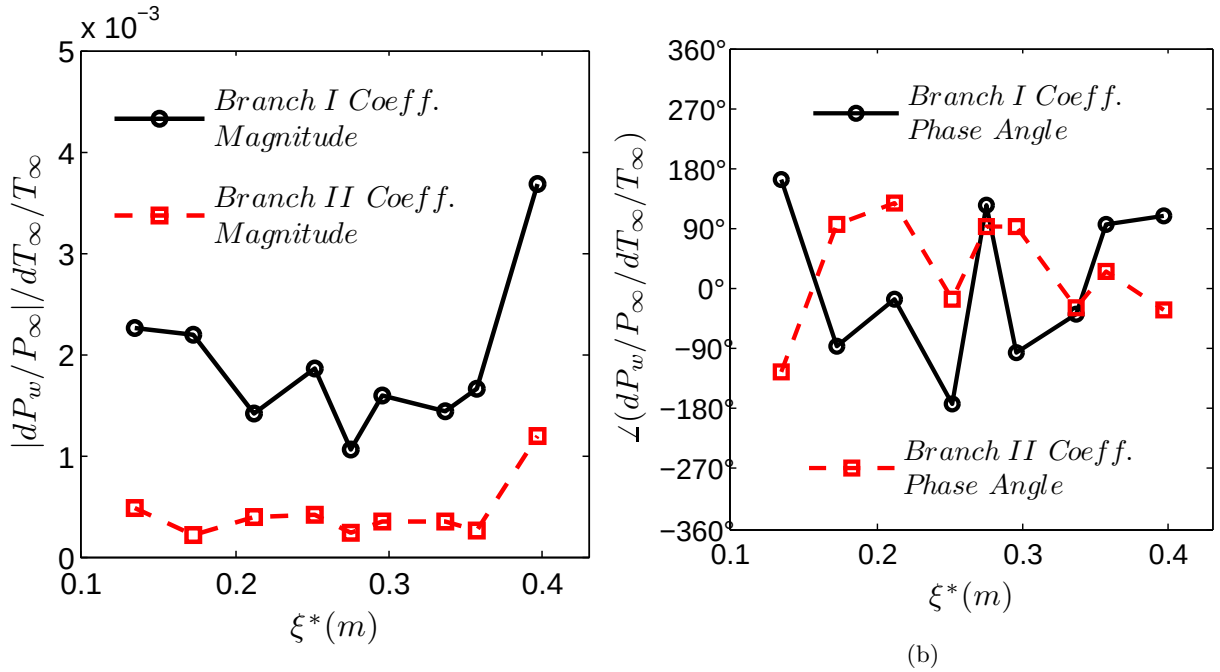

(a) (b)

Figure 35: Phase I and phase II receptivity coefficient magnitudes (a) and phase angles (b) for various locations along the flared cone.

coefficients determined as $C_{recpt} = 4.9\times10^{-3}$ for slow acoustic waves and $C_{recpt} = 9.3\times10^{-3}$ for fast acoustic waves. While our results arise from consideration of receptivity to a freestream entropy perturbation, it was shown here (Figures 25 - 29) and in previous work[1,14] that the interaction of the freestream hotspot with the shock primarily induces acoustic waves behind the shock. The frequencies examined here, however, differ from those examined previously, with the phase I neutral points considered her typically specifying frequencies in the range of 240 kHz to 260 kHz. Regardless, the receptivity coefficients we determine are of the same order as those obtained in the work above via e^N, suggesting some level of agreement between the two methods. The results are thus shown to be reasonable, and the receptivity coefficients are demonstrated to be obtainable for this system via a rigorous method based in the problem's theoretical background.

VI. Conclusion

A multimode decomposition scheme for the analysis of DNS data is implemented. The tool is specified with an eye towards transition prediction via analysis of perturbation amplitudes, with the specific goal of obtaining the receptivity coefficients that characterize a system's response to freestream disturbances. In contrast to prior applications of this method, the tool is herein used to analyze the DNS data for hypersonic flow over a real-world geometry. Where the system has been analyzed by other methods previously, generally good agreement is observed with the current results, and findings of the previous analyses are confirmed. The verification of the implementation and its application further opens the door for consideration of a wide range of future receptivity problems.

The biorthogonal eigenfunction system as specified for a three-dimensional perturbation in a two dimensional boundary layer is first characterized and implemented.[17] It was found that the technique of fundamental solution integration and recombination produced eigenvalues and eigenfunctions that compared well with both prior published results as well as the results of a fourth order compact difference scheme. The method of recombining fundamental solutions to recover continuous spectrum modes was also compared against published results, showing good agreement. The scheme of multimode decomposition was then implemented and tried against signals composed as a sum of modes with known weights. The outputs are compared with the known weights as a measure of the accuracy of the scheme. Verification was also

performed relative to the DNS results to be analyzed, with the discrete mode results of the fundamental solution recombination compared to the values presented from the LST analysis of previous work.

Finally, the method of multimode decomposition was applied to the DNS results, with the weights of the boundary layer discrete modes determined. These results were recombined and compared to the DNS receptivity coefficients as defined, illustrating that the boundary layer discrete modes are of primary importance within the boundary layer itself. The receptivity coefficients for the individual modes were also analyzed across a range of frequencies and locations. This confirmed the prior qualitative/LST analysis' conclusion that the freestream hotspot initially excites the low frequency mode F boundary layer mode, with rapid growth of the mode S disturbance downstream of the mode F/S synchronization point for the most unstable frequency. The receptivity coefficients were further noted to agree in order of magnitude for a previous, similar analysis that utilized the e^N method. Limited continuous spectrum analysis was performed, confirming previous conclusions by showing that the vorticity and entropy modes are of limited importance. The weighted sum of the discrete and continuous modes was compared to the frequency spectrum DNS data for different locations and frequencies, verifying the accuracy of the decomposition. The acoustic spectrum modes were shown to be generally localized outside of the boundary layer, with little influence in the region near the wall. The branch I and branch II receptivity coefficients were also determined for the system. Although exact trends are unclear given the lack of spatial resolution, the coefficients were seen to be fairly constant across the region of analysis relative to nearby values in the mode S frequency spectrum.

The opportunity for future work exists in performing modal decomposition at additional locations along the cone for this case. A finer spatial analysis of the system at hand could help to reveal any hidden trends in the spatial evolution for the receptivity coefficients' magnitudes and especially the phase angles. With a multimode decomposition schema implemented and verified, a more in-depth investigation of receptivity mechanisms for further systems is also enabled. Ultimately, the implementation of this technique in tandem with advanced DNS methods makes the characterization of receptivity problems significantly more manageable, and thus serves as a step forward in the uncovering of pathways by which laminar-turbulent transition takes place.

Appendix A

Given below are the elements corresponding to the matrix $\mathbf{H}_0$ with meanflow pressure included. As in Tumin's 2006[16] and 2007[17] papers, we define $r = 2(\epsilon+2)/3$ and $m = 2(\epsilon-1)/3$, where ϵ is the ratio of bulk viscosity to dynamic viscosity and $\epsilon = 0$ corresponds to Stokes' hypothesis. Coefficients not specified below are to be assumed zero.

$$\chi = \left[\frac{Re}{\mu} - \frac{i\hat{\omega}r}{P}\right]^{-1}$$
$$\hat{\omega} = \omega - \alpha U$$

$$H_0^{1,2} = 1$$
$$H_0^{2,1} = \alpha^2 + \beta^2 - i\hat{\omega}P\gamma M^2\frac{Re}{\mu T}$$
$$H_0^{2,2} = -\frac{1}{\mu}\frac{\partial \mu}{\partial y}$$
$$H_0^{2,3} = -i\alpha\,(m+1)\,\frac{1}{T}\frac{\partial T}{\partial y} - i\alpha\frac{1}{\mu}\frac{\partial \mu}{\partial y} + RePM^2\frac{1}{\mu T}\frac{\partial U}{\partial y} + i\alpha\,(m+1)\,\frac{1}{P}\frac{\partial P}{\partial y}$$
$$H_0^{2,4} = i\alpha\frac{Re}{\mu} + \alpha\hat{\omega}\,(m+1)\,\frac{1}{P}$$
$$H_0^{2,5} = -\alpha\hat{\omega}\,(m+1)\,\frac{1}{T} - \frac{1}{\mu}\left(\frac{\partial T}{\partial y}\frac{\partial U}{\partial y}\frac{\partial^2 \mu}{\partial T^2} + \frac{\partial \mu}{\partial T}\frac{\partial^2 U}{\partial y^2}\right)$$
$$H_0^{2,6} = -\frac{1}{\mu}\frac{\partial \mu}{\partial T}\frac{\partial U}{\partial y}$$

$$H_0^{3,1} = -i\alpha$$
$$H_0^{3,3} = \frac{1}{T}\frac{\partial T}{\partial y} - \frac{1}{P}\frac{\partial P}{\partial y}$$
$$H_0^{3,4} = \frac{i\hat{\omega}}{P}$$
$$H_0^{3,5} = -\frac{i\hat{\omega}}{T}$$
$$H_0^{3,7} = -i\beta$$
$$H_0^{4,1} = -i\chi\alpha\left(r\frac{1}{T}\frac{\partial T}{\partial y} + \frac{2}{\mu}\frac{\partial \mu}{\partial y} - r\frac{1}{P}\frac{\partial P}{\partial y}\right)$$
$$H_0^{4,2} = -i\chi\alpha$$
$$H_0^{4,3} = \chi\left(-\alpha^2 - \beta^2 + i\hat{\omega}P\gamma M^2\frac{Re}{\mu T} + r\frac{1}{T}\frac{\partial^2 T}{\partial y^2} + r\frac{1}{\mu T}\frac{\partial \mu}{\partial y}\frac{\partial T}{\partial y} - r\frac{1}{\mu P}\frac{\partial \mu}{\partial y}\frac{\partial P}{\partial y} + 2r\frac{1}{P^2}\left[\frac{\partial P}{\partial y}\right]^2 - 2r\frac{1}{PT}\frac{\partial P}{\partial y}\frac{\partial T}{\partial y} - r\frac{1}{P}\frac{\partial^2 P}{\partial y^2}\right)$$
$$H_0^{4,4} = -i\chi r\frac{1}{P}\left(\alpha\frac{\partial U}{\partial y} - \hat{\omega}\frac{1}{T}\frac{\partial T}{\partial y} - \hat{\omega}\frac{1}{\mu}\frac{\partial \mu}{\partial y} + 2\hat{\omega}\frac{1}{PT}\frac{\partial P}{\partial y}\right)$$
$$H_0^{4,5} = i\chi\left(\alpha r\frac{1}{T}\frac{\partial U}{\partial y} + \alpha\frac{1}{\mu}\frac{\partial \mu}{\partial T}\frac{\partial U}{\partial y} - r\hat{\omega}\frac{1}{\mu T}\frac{\partial \mu}{\partial y} + r\hat{\omega}\frac{1}{PT}\frac{\partial P}{\partial y}\right)$$
$$H_0^{4,6} = -i\chi r\hat{\omega}\frac{1}{T}$$
$$H_0^{4,7} = -i\chi\beta\left(r\frac{1}{T}\frac{\partial T}{\partial y} + 2\frac{1}{\mu}\frac{\partial \mu}{\partial y} - r\frac{1}{P}\frac{\partial P}{\partial y}\right)$$
$$H_0^{4,8} = -i\chi\beta$$
$$H_0^{5,6} = 1$$
$$H_0^{6,2} = -2\left(\gamma - 1\right)M^2 Pr\frac{\partial U}{\partial y}$$
$$H_0^{6,3} = -2i\alpha\left(\gamma - 1\right)M^2 Pr\frac{\partial U}{\partial y} + P\gamma M^2 Pr\frac{Re}{\mu T}\frac{\partial T}{\partial y} - \left(\gamma - 1\right)M^2 Pr\frac{Re}{\mu}\frac{\partial P}{\partial y}$$
$$H_0^{6,4} = i\hat{\omega}\left(\gamma - 1\right)M^2 Pr\frac{Re}{\mu}$$
$$H_0^{6,5} = \alpha^2 + \beta^2 - i\hat{\omega}P\gamma M^2 Pr\frac{Re}{\mu T} - \left(\gamma - 1\right)M^2 Pr\frac{1}{\mu}\frac{\partial \mu}{\partial T}\left(\frac{\partial U}{\partial y}\right)^2 - \frac{1}{\mu}\frac{\partial^2 \mu}{\partial y^2}$$
$$H_0^{6,6} = -\frac{2}{\mu}\frac{\partial \mu}{\partial y}$$
$$H_0^{7,8} = 1$$
$$H_0^{8,3} = -i\beta\left(m + 1\right)\frac{1}{T}\frac{\partial T}{\partial y} - i\beta\frac{1}{\mu}\partial\mu\partial y + i\beta\left(m + 1\right)\frac{1}{P}\frac{\partial P}{\partial y}$$
$$H_0^{8,4} = \beta\hat{\omega}\left(m + 1\right)\frac{1}{P} + i\beta\frac{Re}{\mu}$$
$$H_0^{8,5} = -\beta\hat{\omega}\left(m + 1\right)\frac{1}{T}$$
$$H_0^{8,7} = \alpha^2 + \beta^2 - i\hat{\omega}P\gamma M^2\frac{Re}{\mu T}$$
$$H_0^{8,8} = -\frac{1}{\mu}\frac{\partial \mu}{\partial y}$$

Acknowledgments

This work was sponsored by the Air Force Office of Scientific Research, USAF, under Grant No. FA9550-15-1-0268, first monitored by Dr. Rengasamy Ponnappan, and now by Dr. Ivett Leyva. The views and conclusions contained herein are those of the authors and should not be interpreted as necessarily representing the official policies or endorsements either expressed or implied, of the Air Force Office of Scientific Research or the U.S. Government.

References

[1]Ma, Y., Zhong, X., *Receptivity of a Supersonic Boundary Layer over a Flat Plate. Part 3. Effects of Different Types of Free-stream Disturbances*, Journal of Fluid Mechanics, vol. 532, pp. 63-109. December 2004.

[2]Reshotko E., *Hypersonic Stability and Transition*, Hypersonic Flows for Reentry Problems, Berlin: Springer, 1991.

[3]Zhong, X., Lee, T.K., *Nonequilibrium Real-Gas Effects on Disturbance/Bow Shock Interaction in Hypersonic Flow Past a Cylinder*, AIAA, 1996.

[4]Zhong, X., *Receptivity of Mach 6 Flow over a Flared Cone to Freestream Disturbance*, AIAA Paper, 2004-253, January 2004.

[5]Mack, L.M., *Boundary Layer Linear Stability Theory*, AGARD report, No. 709, pp.3-1 to 3-81, 1984.

[6]Kovasznay, L. S. G., *Turbulence in Supersonic Flow*, Journal of the Aeronautical Sciences, Vol. 20, No. 10, pp. 657-682, October 1953.

[7]McKenzie, J. F., Westphal, K. O., *Interaction of Linear Waves with Oblique Shock Waves*, The Physics of Fluids, Vol. 11, No. 11, November 1968.

[8]Salyer, T.R., *Laser Differential Interferometry for Supersonic Blunt Body Receptivity Experiments*, PhD Thesis, Purdue University, May 2002.

[9]Salyer, T.R., Collicott, S.H., Schneider, S.P., *Characterizing Laser-Generated Hot Spots for Receptivity Studies*, AIAA Journal, Vol.44, No.12, December 2006.

[10]Schneider, S.P., Wheaton, B.M., Julinao, T.J., Berridge, D.C., Chou, A., Gilbert P.L., Casper. K.M., Steen, L.E., *Instability and Transition Measurements in the Mach-6 Quiet Tunnel*, AIAA Paper, 2009-3559, June 2009.

[11]Huang, Y., Zhong, X., *Numerical Study of Laser-Spot Effects on Boundary-Layer Receptivity for Blunt Compression-Cones in Mach-6 Freestream*, AIAA paper, 2010-4447, June 2010.

[12]Schmisseur, J.D., Collicott, S.H., Schneider, S.P., *Laser-Generated Localized Freestream Perturbations in Supersonic and Hypersonic Flows*, AIAA Journal, vol. 38, No.4, April 2000.

[13]Huang, Y., Zhong, X., *Numerical Study of Freestream Hot-Spot Perturbation on Boundary-Layer Receptivity for Blunt Compression-Cones in Mach-6 Flow*, AIAA paper, 2011-3078, June 2011.

[14]Huang, Y., Zhong, X. *Numerical Study of Hypersonic Boundary-Layer Receptivity with Freestream Hotspot Perturbations*, AIAA Journal, Vol.52, No.12, December 2014.

[15]Tumin, A. M., Fedorov, A. V., *Spatial growth of disturbances in a compressible boundary layer*, J. Appl. Mech. Tech. Phys. 24, 548 1983.

[16]Tumin, A. M., *Three-Dimensional Spatial Normal Modes in Compressible Boundary Layers*, AIAA paper, 2006-1109, January 2006.

[17]Tumin, A. M., *Three-Dimensional Spatial Normal Modes in Compressible Boundary Layers*, Journal of Fluid Mechanics, vol. 586, pp. 295-322. April 2007.

[18]Tumin, A., Wang, X., Zhong, X., *Direct Numerical Simulation and the Theory of Receptivity in a Hypersonic Boundary Layer*, Physics of Fluids, Vol. 19, 014101, January 2007.

[19]Denissen, N. A., White, E. B., *Continuous spectrum analysis of roughness-induced transient growth*, Physics of Fluids, Vol. 21, 114105, November 2009

[20]Zhong, X. *High-Order Finite-Difference Schemes for Numerical Simulation of Hypersonic Boundary-Layer Transition*, Journal of Computational Physics 144,662-709, April 1998.

[21]Dunn, J.W., *Numerical Simulation of Bow-Shock/Disturbance Interactions in Mach-4 Flows Past a Hemisphere*, AIAA Paper, 98-0007, January 1998.

[22]Press et al, *Numerical Recipes The Art of Scientific Computing*, Cambridge University Press 1986.

[23]Hefferon, J., *Linear Algebra*, Orthogonal Publishing L3C, 2015

[24]Malik, M. R., *Numerical Method for Hypersonic Boundary Layer Stability*, Journal of Computational Physics, 86, 376-413, 1990.

[25]Rice, J. R., *Experiments on Gram-Schmidt orthogonalization*, Math. Comp., 20:325-328, 1966.

[26]Balakumar, P. and Malik, M. R., *Discrete modes and continuous spectra in supersonic boundary layer*, J. Fluid Mech., Vol. 239, 1992, pp. 631-656.

[27]Fedorov, V. A., and Khokhlov, A. P., *Prehistory of Instability in a Hypersonic Boundary Layer*, Theoretical and Computational Fluid Dynamics, Vol. 14, No. 6, 2001, pp. 359375.

[28]Balakumar, P., and Kegerise, M. A., *Receptivity of Hypersonic Boundary Layers over Straight and Flared Cones*, AIAA Paper 2010-1545, January 2010.

[29]Saric, S. S., Reed, H. L., Kerschen, E. J., *Boundary-Layer Receptivity to Freestream Disturbances*, Annu. Rev. Fluid Mech, 34:291-319, 2002.